Separation of source, attenuation and site parameters of 2 moderate earthquakes in France: an elastic radiative transfer approach

Grégoire Heller, Ludovic Margerin, Olivier Sèbe, Jessie Mayor, Marie Calvet, Paola Traversa, Soumaya Latour

Geophysical Journal International

Geophys. J. Int. (2024) **238,** 700–718
Advance Access publication 2024 May 20
GJI Seismology

https://doi.org/10.1093/gji/ggae176

Separation of source, attenuation and site parameters of 2 moderate earthquakes in France: an elastic radiative transfer approach

G. Heller [1,2] L. Margerin,[1] O. Sèbe,[2] J. Mayor,[3] M. Calvet,[1] P. Traversa[3] and S. Latour[1]

[1]*Institut de Recherche en Astrophysique et Planétologie, Observatoire Midi-Pyrénées, Université Paul Sabatier, C.N.R.S.,* 14 *Avenue Edouard Belin, OMP 31400 Toulouse, France. E-mail: greg68heller@hotmail.fr*
[2]*CEA, DAM, DIF, F-*91297 *Arpajon, France*
[3]*EDF DT-TEGG,* 180 *rue du lieutenant Parayre* 13290 *Aix-en-Provence, France*

Accepted 2024 May 7. Received 2024 April 11; in original form 2023 July 28

SUMMARY

An accurate magnitude estimation is necessary to properly evaluate seismic hazard, especially in low to moderate seismicity areas such as Metropolitan France. However, magnitudes of small earthquakes are subject to large uncertainties caused by major high-frequency propagation effects which are generally not properly considered. To address this issue, we developed a method to separate source, attenuation and site parameters from the elastic radiative transfer modelling of the full energy envelopes of seismograms. The key feature of our approach is the treatment of attenuation—both scattering and absorption—in a simple but realistic velocity model of the Earth's lithosphere, including a velocity discontinuity at the Moho. To reach this goal, we developed a 2-step inversion procedure, allowing first to extract attenuation parameters for each source-station path from the whole observed energy envelope using the Levenberg–Marquardt and grid-search algorithms, then to determine site amplification and the source displacement spectrum from which the moment magnitude M_w is extracted. In the first step, we use the forward modelling procedure of Heller *et al.* in order to simulate energy envelopes by taking into account the full treatment of wave polarization, the focal mechanism of the source and the scattering anisotropy. The inversion procedure is then applied to the 2019 M_L 5.2 Le Teil and 2014 M_L 4.5 Lourdes earthquakes which both occurred in southern France. Data from 6 stations are selected for each event. The inversion results confirm a significant variability in the attenuation parameters (scattering and absorption) at regional scale and a strong frequency dependence. Scattering appears to be stronger towards the French Alps and Western Pyrenees. Absorption is stronger as frequency increases. Although not very resolvable, the mechanism of scattering appears to be forward or very forward. By inverting the source spectrum, we determine moment magnitudes M_w of 5.02 $\pm$ 0.17 for the Le Teil earthquake and 4.17 $\pm$ 0.15 for the Lourdes earthquake.

Key words: Numerical modelling; Coda waves; Seismic attenuation; Wave propagation; Wave scattering and diffraction.

1 INTRODUCTION

An accurate estimation of earthquake magnitude and seismic attenuation properties is necessary to assess seismic hazard. For example, magnitudes are necessary to calibrate the Gutenberg–Richter law or ground motion prediction equations (see e.g. Baker *et al.* 2021). The two most common magnitude scales are (1) the moment magnitude M_w, computed from the seismic moment M_0 (Kanamori 1977), which is directly related to the plateau of the source spectrum at low frequencies and (2) the local magnitude, which is empirically computed from the logarithm of the maximum amplitude of the signal (Richter 1935). As M_0 can be related to a physical model of fault rupture, M_w is considered to be the most relevant magnitude scale to quantify earthquake size. Unfortunately, the determination of M_w is either difficult or impossible for small earthquakes, because the low frequencies radiated by the source are buried in the ambient noise. As a consequence, one must rely on the high-frequency content of seismograms, which is particularly difficult to model since it is affected by complex propagation effects caused by the presence of poorly known geological heterogeneities.

As an alternative, the M_L scale (or another empirical scale) is typically used to compute the magnitude of small earthquakes (e.g. Shelly *et al.* 2021). To homogenize the magnitude scale, M_L can be converted to M_w using an empirical linear relationship (e.g.

Braunmiller *et al.* 2005; Cara *et al.* 2015). The drawback of this approach is that the M_L scale is often imprecise. Furthermore, it may suffer from undetected biases, due to the lack of knowledge on the regional propagation. This issue is acute in the case of France, where the assessment of seismic hazard is mainly based on small earthquakes for which mostly local magnitudes have been determined. Currently, there remain large inconsistencies between different earthquake magnitude estimations, especially between M_L and M_w (Braunmiller *et al.* 2005; Deichmann 2006; Cara *et al.* 2017; Shelly *et al.* 2021), which sometimes exceed 1 in magnitude scale (Sira *et al.* 2016)

We propose that inconsistencies in M_L estimations in France could be explained to a large extent by regional variations of attenuation properties, as highlighted by previous studies (Campillo & Plantet 1991; Sens-Schönfelder *et al.* 2009; Calvet *et al.* 2013; Denieul *et al.* 2015; Mayor *et al.* 2016, 2018). More specifically, Mayor *et al.* (2018) found that regional variations of intrinsic attenuation $({}^{S}Q_i)^{-1}$ could reach ± 50 per cent across the country, in all frequency bands between 1 and 32 Hz. These variations are currently not incorporated into M_L estimations in France. As a consequence, magnitudes may be underestimated in high-attenuation zones (Mediterranean Basin, Aquitaine Basin, Parisian Basin, Rhône Valley) and overestimated in low attenuation zones (Armorican Massif, Central Massif and Ardennes). This interpretation is corroborated by the findings of Mayor *et al.* (2018) who identified an apparent dependence of $({}^{S}Q_i)^{-1}$ with respect to magnitude for small events in France. These preliminary remarks point to the fact that the relative contributions of attenuation and source to the measured ground motions are still not well separated. Furthermore magnitudes of small earthquakes may be systematically biased by the imprecise modelling of attenuation.

As outlined above, classical methods like moment tensor determination from waveform modelling (e.g. Braunmiller *et al.* 2002) demand that the low-frequency content of seismogram be sufficiently energetic. In Metropolitan France, this property typically breaks down for $M_w \leq 3 - 3.5$. As an alternative to the modelling of direct waves, a number of studies have suggested that the specific characteristics of coda waves could facilitate the separation of source, site and path effects, thereby allowing the recovery of earthquake magnitude from high-frequency ground motions. We now provide a short and by no means complete review of these studies.

Since the pioneering work of Aki & Chouet (1975), it has been observed worldwide that the energy in the seismic coda is correlated with the source size, independent of the relative location of the source and station in a given region. This remarkable property may be formalized with the aid of the coda normalization principle. It stipulates that in a small frequency band, the energy contained in a late time window ($[T, T + \Delta T]$) in the coda is proportional to the energy injected by the source and to the site amplification factor but is independent of other factors such as the epicentral distance or the source mechanism. The key point is that the lapse-time T is the same for all events in a given region. The coda normalization principle has been intensely exploited to extract the source and site terms (Rautian & Khalturin 1978; Tsujiura 1978; Aki 1980). Nevertheless, its application can become inconvenient in regions with strong spatial variations of attenuation properties. To circumvent the difficulty, Wang & Shearer (2019) introduce path dependent attenuation properties for coda waves, while retaining the general idea that the coda level is proportional to the source and site terms. Elaborating on the work of Mayeda & Walter (1996), Mayeda *et al.* (2003) developed a parametric and entirely empirical approach to correct for attenuation properties. This strategy allowed them to calibrate a distance dependent model of *S*-wave envelope shape for a given region, and to calibrate magnitudes of small to moderate earthquakes. The method of Mayeda *et al.* (2003) has been improved later on to take into account the lateral variations of attenuation (Pasyanos *et al.* 2016). To exploit seismograms from the pre-digital era, Denieul *et al.* (2015) calibrated envelope shapes in the temporal domain and took into account large regional variations of attenuation, before extracting magnitudes in Metropolitan France.

The approaches presented so far are empirical and rely on *ad hoc* assumptions -for instance the analytical form adopted to model envelopes- which are not easily justified theoretically and require empirical corrections to be applied to the data. In addition, we note that attenuation effects are removed without being quantified. To dispense with such assumptions, physical approaches to model wave propagation have been developed. The approach of Takahashi *et al.* (2005) is based on a simple physical model of propagation for direct *S* waves and separates site and attenuation effects by a coda normalization approach. The source parameter is then retrieved from corrected earthquake spectra. In terms of physical modelling, an important contribution was made by Sens-Schönfelder & Wegler (2006). These authors developed a 2-step inversion procedure to separate source, attenuation and site parameters by modelling the energy envelopes of *S* waves using radiative transfer theory. The key point of this approach is that the shape of the envelope is not hypothesized a priori. Instead, the strength of scattering and intrinsic attenuation are adjusted to match the observed envelopes as closely as possible. This allows one to isolate the propagation term and offers an estimate of the crustal attenuation parameters as a by-product.

The inversion procedure of Sens-Schönfelder & Wegler (2006) has later been improved and automated by Eulenfeld & Wegler (2016) which facilitated the application to several regions in the world (Eulenfeld & Wegler 2017; Eken 2019; Eulenfeld *et al.* 2022). These recent developments based on multiple-scattering theory still rely on assumptions and simplifications of the physics—acoustic approximation, uniform half-space and isotropic scattering—that are questionable. It is for example well established that a velocity contrast such as the Moho, strongly influences the amplitude and shape of seismogram envelopes (e.g. Margerin *et al.* 1998; Heller *et al.* 2022). On the one hand, leakage of seismic energy from crust to mantle can significantly increase the coda decay rate (Margerin *et al.* 1999). On the other hand, the *S*-energy trapped in the crust gives rise to a prominent *Lg* phase at regional propagation distance. Consequently, taking into account the stratification of velocity and attenuation of the lithosphere is important to synthesize realistic seismogram envelopes. We refer the reader to the introduction of Heller *et al.* (2022) for theoretical developments on the radiative transfer theory.

Elaborating on the recent work of Eulenfeld & Wegler (2016) and Eulenfeld *et al.* (2022), we present a radiative transfer approach to separate source from attenuation and site parameters using high-frequency seismogram envelopes. The forward modelling follows Heller *et al.* (2022) and features a complete treatment of polarization effects for source radiation, scattering by small-scale inhomogeneities and reflections at crustal boundaries. This allows us to synthesize realistic seismogram envelopes including the main crustal phases and their codas. The modelling tool has been incorporated in a 2-step procedure to separate regional propagation, source and site effects, based on the inversion of full seismogram

envelopes. The method is illustrated by an application to two moderate regional earthquakes recorded in metropolitan France, for which independent magnitude estimates are available and comparison of regional attenuation parameters with independent studies (Campillo & Plantet 1991; Lacombe *et al.* 2003; Sens-Schönfelder *et al.* 2009; Drouet *et al.* 2010; Calvet & Margerin 2013; Mayor *et al.* 2018) is possible.

The paper is organized as follows. In Section 2, we present the data of the two events considered in this study: the 2019 M_L 5.2 Le Teil earthquake and 2014 M_L 4.5 Lourdes earthquake. In Section 3, we briefly present the physical model of wave propagation in an inhomogeneous lithosphere and recall the main elements of the algorithm used to simulate energy envelopes. Next, we explain in some details the 2-step inversion procedure focusing on the separation of attenuation from source and site effects. Section 4 presents the inversion results for the selected earthquakes and Section 5 concludes.

2 REGIONAL SETTING AND DATA SELECTION

The 2019 M_L 5.2 Le Teil and 2014 M_L 4.5 Lourdes earthquakes are two moderate seismic events which occurred, respectively, in Southeastern France near the Rhone Valley and in the French Pyrenees (see Fig. 1a). The Le Teil earthquake has been the most significant earthquake in metropolitan France in the period 2010–2019 (Duverger *et al.* 2021) and caused significant damages near the epicentre (Schlupp *et al.* 2021). While the Le Teil event affected a region of low seismicity (Ampuero *et al.* 2020), the Lourdes earthquake took place in the most tectonically active region of the Pyrenees (Souriau *et al.* 2014). We selected these two events to illustrate our inversion procedure because high-quality waveforms were recorded at local to regional distances from each epicentre, offering good azimuthal coverage. This allows us to explore path effects across regions with diverse geological properties.

Previous studies highlighted significant regional variations of attenuation in France (Campillo & Plantet 1991; Sens-Schönfelder *et al.* 2009; Calvet *et al.* 2013; Denieul *et al.* 2015; Mayor *et al.* 2016, 2018). Recent investigations confirm that the variability of the shapes of seismogram envelopes cannot be explained by a unique attenuation model in France (Heller 2021, p. 117). Hence, to separate efficiently path from source and site effects, it is important to take into account lateral variations of attenuation properties. To address this point, we propose a path-based inversion procedure which is presented in the next section. The method is subsequently applied to data from six carefully selected stations for each of the Le Teil and Lourdes earthquakes (Figs 1b and c). The choice ensures a good azimuthal coverage and explores a variety of lithological and tectonic environments. Thanks to the relatively short epicentral distances in our data set, the seismograms do not show distinguishable mantellic phases such as *Pn* and *Sn*. The dominantly crustal propagation simplifies the modelling considerably. All traces show good signal-to-noise ratio in all frequency bands and the selected stations are not affected by strong site effects. The absence of significant amplifications has been verified by application of the coda normalization approach (Phillips & Aki 1986) and by inspection of the H/V ratios in the coda (Margerin *et al.* 2009).

Seismic data were downloaded from the RESIF portal (Réseau Sismologique et géodésique français) and consist of recordings from the french broad-band and accelerometric permanent networks (RLBP, Réseau Large-Bande Permanent; RAP, Réseau Accélérométrique Permanent; GEOSCOPE network, (RESIF 1995a, b; Romanowicz *et al.* 1984)) and temporary experiments (PYROPE, Chevrot *et al.* 2017). To construct the energy envelopes, the seismic traces are first converted to velocigrams. Selected velocigrams are shown in Figs 1(d) and (e) for both earthquakes. Next, two-poles Butterworth bandpass filters are applied to the data in 7 octave-wide frequency bands centred at $f_0 = 0.375$, 0.75, 1.5, 3, 6, 12 and 24 Hz. At each frequency f_0, the energy envelope of earthquake i recorded at station j, denoted $E^{ij}_{\rm obs}(t, f_0)$, is calculated from the three components of the filtered velocigrams $\dot{u}^{ij}_k(t, f_0)$ as follows:

$$E^{ij}_{\rm obs}(t, f_0) = \frac{\rho_j \langle \dot{u}^{ij}(t, f_0)^2 \rangle}{2\Delta f}, \tag{1}$$

where ρ_j is the average density of the crust at the station set at 2800 kg m^{-3}. The quantity $\dot{u}^{ij}(t, f_0)^2$ denotes the squared analytic signal summed over the three components (Sato *et al.* 2012, p. 41):

$$\dot{u}^{ij}(t, f_0)^2 = \frac{1}{2}\sum_{k=1}^{3}\left(\dot{u}^{ij}_k(t, f_0)^2 + \mathcal{H}\left[\dot{u}^{ij}_k(t, f_0)\right]^2\right), \tag{2}$$

where $\mathcal{H}$ denotes the Hilbert transform. In eq. (1), the brackets $\langle \cdot \rangle$ indicate smoothing by a moving average window. To obtain a good compromise between reduction of envelope fluctuations and temporal resolution, we found it convenient to adapt the width of the moving window to the central frequency: four cycles for $f_0 \leq 0.75$ Hz, eight cycles for $1.5 \leq f_0 \leq 3$ Hz and 16 cycles for $f_0 \geq 6$ Hz. Normalization of the kinetic energy by the filter bandwidth Δf in eq. (1) yields a spectral energy density that can be quantitatively compared to the predictions of radiative transfer theory. In the next section, the stochastic description of the medium and the simulation algorithm are briefly outlined.

3 METHOD

3.1 Energy transport model

3.1.1 *Random medium characteristics*

We consider a simple, realistic model of the Earth's lithosphere, consisting of a multiple-scattering crust overlying a homogeneous mantle (see Fig. 2). Crust and mantle are separated by a horizontal velocity contrast (Moho) at a depth H, where the energy can either be reflected or transmitted. A free surface delimits the top of the crust, where total reflection occurs. We suppose for simplicity that the probability for a mantle-transmitted wave to return to the crust is negligible. In reality, the mantle does contain heterogeneities (e.g. Lee *et al.* 2003; Mancinelli *et al.* 2016). However, they are so much weaker than the one contained in the crust that backscattering from the mantle may be neglected, at least on the local to regional scale. As a consequence, the crustal energy can only decrease exponentially over time even without absorption. This phenomenon has been called energy leakage in the literature (Korn 1990; Margerin *et al.* 1998).

In our model, the crust consists of a continuous random medium with correlated fluctuations of velocity and density $\delta\alpha$, $\delta\beta$ and $\delta\rho$, superimposed on a homogeneous background characterized by the mean velocities α, β and density ρ. The fluctuations $\delta\alpha$, $\delta\beta$ and $\delta\rho$ are related by Birch's law:

$$\frac{\delta\alpha}{\alpha} = \frac{\delta\beta}{\beta} = \frac{1}{\nu}\frac{\delta\rho}{\rho} \tag{3}$$

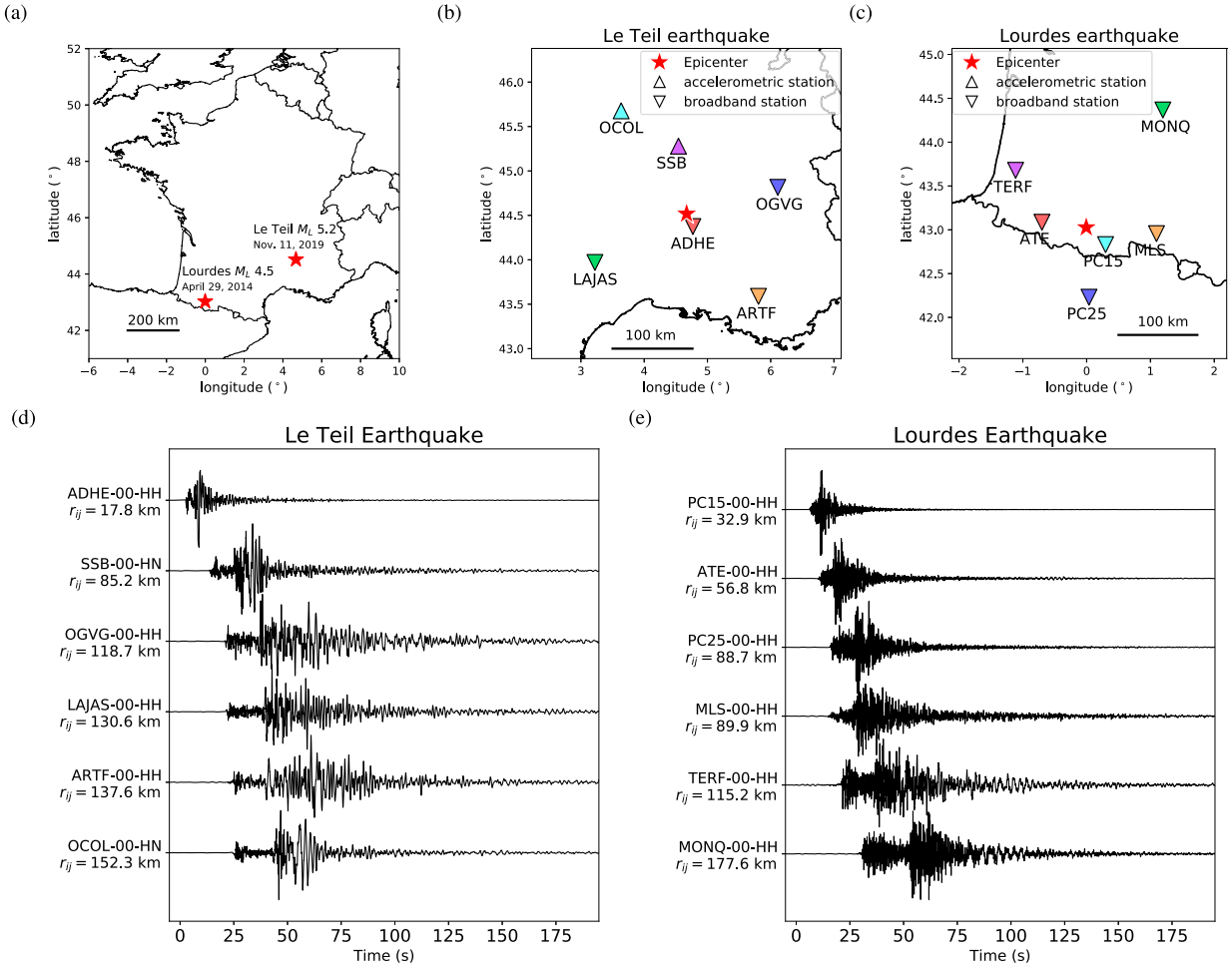

Figure 1. (a) Location of the 2019 M_L 5.2 Le Teil and 2014 M_L 4.5 Lourdes events. (b) Locations of the six stations selected for the Le Teil earthquake. (c) Locations of the six stations selected for the Lourdes earthquake. (d) Selected raw velocity seismograms (vertical components) for the Le Teil earthquake. (e) Selected raw velocity seismograms (vertical components) for the Lourdes earthquake. For the Le Teil earthquake, 3-component raw and filtered seismograms are shown in Figs S1–S6. For filtered seismograms, central frequencies are $f_0 = 0.75$ and 3.0 Hz.

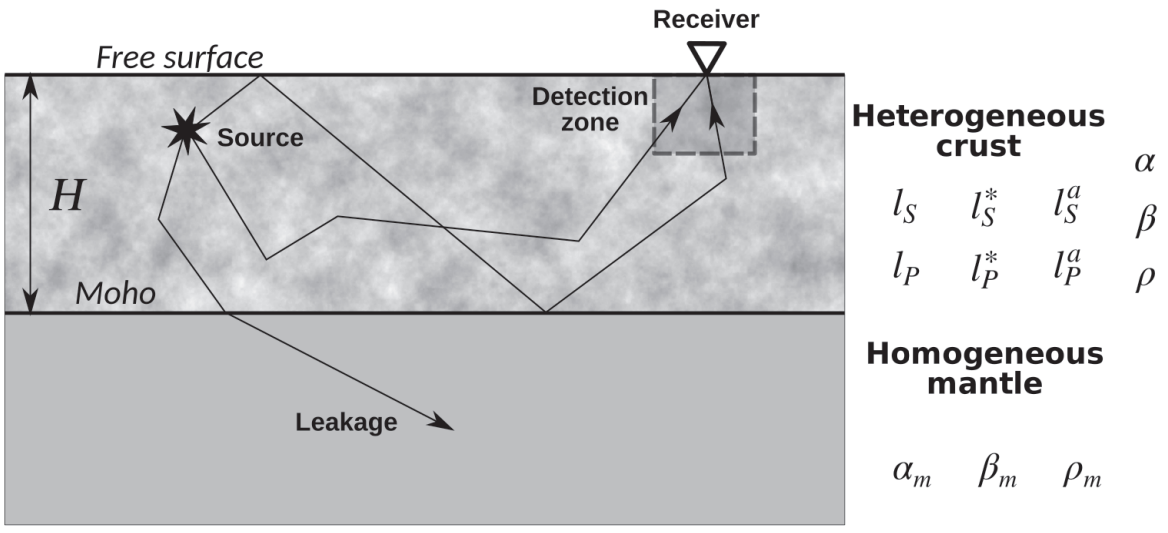

Figure 2. Model geometry and parameters of the Monte Carlo simulations.

with parameter $\nu = 0.8$ as suggested for lithospheric rocks (Sato 1984). Furthermore, we suppose that the spatial correlation $R(r)$ of the fluctuations is described by an exponential function:

$$R(r) = \epsilon^2 \exp(-r/l_c), \tag{4}$$

where r is the distance between 2 points in the medium, ϵ^2 the amplitudes of the fluctuations and l_c the correlation length, which quantifies the characteristic size of small-scale inhomogeneities. [See Sato *et al.* (2012) and Sato (2019) for a review of stochastic properties of crustal materials.]

3.1.2 Scattering and attenuation length scales

In the heterogeneous crust, we use radiative transfer theory for polarized elastic waves (Weaver 1990; Ryzhik *et al.* 1996; Margerin 2005) to model the transport of seismic energy. We refer to Heller *et al.* (2022) for a detailed discussion of the treatment of scattering by small inhomogeneities and reflection/transmission at crustal boundaries for polarized elastic waves using the Stokes vector formalism.

In the crust, the coherent wave attenuation due to scattering by small-scale heterogeneities is quantified by the mean free paths of P and S waves l_P and l_S, which also represent the average distance between two scattering events for each wave type. For fixed correlation function (exponential in our case) and Birch parameter ν, these length scales depend only on the ratio l_c/λ (λ the wavelength of the incident waves) and the ratio between the variance of the fluctuations and the correlation length ϵ^2/l_c. As shown by (e.g. Sato 1984; Weaver 1990), l_P and l_S may be readily evaluated based on the Born approximation. In the multiple scattering regime, the key length scales that characterize the attenuation and coda generation are the transport mean free paths l_P^* and l_S^* (e.g. Gusev & Abubakirov 1999; Gaebler *et al.* 2015; Celorio *et al.* 2022). l_P^* and l_S^* can be understood as the average distance over which a beam of waves loses 'memory' of its initial direction of propagation as a consequence of multiple non-isotropic events (e.g. Margerin *et al.* 1998; Turner 1998). Similar to l_P and l_S, the transport mean free paths are functions of l_c/λ and ϵ^2/l_c.

The ratio l^*/l quantifies the anisotropy of the scattering and depends critically on the non-dimensional parameter l_c/λ. Predominantly forward (resp. backward) scattering corresponds to $l^*/l > 1$ (resp $l^*/l < 1$). For elastic waves in a weakly inhomogeneous medium, backward scattering is possible only in the propagation regime $l_c/\lambda \ll 1$, while forward scattering prevails when λ is of the order of, or less than l_c.

Because the Earth is imperfectly elastic, the total seismic energy decays exponentially with time. The spatial rate of decay of P and S waves can be quantified by the absorption lengths l_P^a and l_S^a, respectively. As usual, we assume that absorption is solely caused by shear deformation implying $l_P^a/l_S^a = \frac{3}{4}(\alpha/\beta)^3$ (adapted from e.g. Shearer 1999, p. 114).

To make the link with seismological practice, it is convenient to introduce scattering and intrinsic quality factors for S waves ${}^S Q_{sc}^*$ and ${}^S Q_i$ which are related to the transport mean free path and absorption length by the following relationships (adapted from Eulenfeld & Wegler 2016):

$$\begin{aligned} {}^S Q_{sc}^* &= \frac{2\pi f l_S^*}{\beta} \\ {}^S Q_i &= \frac{2\pi f l_S^a}{\beta}. \end{aligned} \tag{5}$$

Note that we define ${}^S Q_{sc}^*$ in terms of the transport mean free path l_S^* rather than the scattering mean free path l_S. The reason is that the former is the appropriate attenuation length scale for the peak intensity observed in a typical realization of a random medium, whereas the latter quantifies specifically the attenuation of the coherent ensemble-averaged wave which is inaccessible in seismic experiments (see Celorio *et al.* 2022, for numerical examples and further discussion). We also introduce the total (or extinction) quality factor for S waves ${}^S Q_e$:

$$\left({}^S Q_e\right)^{-1} = \left({}^S Q_{sc}^*\right)^{-1} + \left({}^S Q_i\right)^{-1}. \tag{6}$$

We also introduce the seismic albedo B, defined as the ratio of scattering attenuation to total attenuation for S waves:

$$B = \frac{\left(l_S^*\right)^{-1}}{\left(l_S^*\right)^{-1} + \left(l_S^a\right)^{-1}}. \tag{7}$$

3.1.3 Parametrization

Assuming a Birch coefficient $\nu = 0.8$ and an exponential correlation function, the three parameters l_c, ϵ^2 and ${}^S Q_i$ completely specify the scattering and attenuation properties of the crust at a given central frequency f_0. However, this parametrization is inconvenient for the inverse problem because it combines dimensional and non-dimensional quantities. Furthermore, a change of l_c perturbs simultaneously the scattering pattern and the scattering mean free path, which complicates the computation of partial derivatives of envelopes needed for linearized inversions. As an alternative, we find it convenient to use the attenuations (expressed in inverse time) $\mu_S = \beta/l_S$, $\mu_S^* = \beta/l_S^*$ and $\mu_S^a = \beta/l_S^a$ as the fundamental set of parameters characterizing the random medium. At a given frequency, l_c is completely determined by the ratio μ_S/μ_S^* and ϵ^2 is in turn determined by the magnitude of μ_S (or μ_S^*). Note that the P mean free paths and absorption lengths are *not* free parameters: they are entirely determined by the triplet $(\mu_S, \mu_S^*, \mu_S^a)$ thanks to the assumptions listed in Sections 3.1.1 and 3.1.2 and the equations of Sato *et al.* (2012).

3.2 Synthetic envelopes computation

We express the modelled energy envelopes $E_{\text{mod}}^{ij}(t, f_0)$ in the following form:

$$E_{\text{mod}}^{ij}(t, f_0) = W_i(f_0) R_j(f_0) G_{ij}(t, f_0, l_S, l_S^*, l_S^a), \tag{8}$$

where $W_i(f_0)$ is the spectral source energy for earthquake i, $R_j(f_0)$ is the site term expressed in energy for station j and $G_{ij}(t, f_0, l_S, l_S^*, l_S^a)$ is the energy propagation term for a unit source. It can be understood as a Green's function of the radiative transfer equation, although this term might be a bit misleading since G_{ij} takes into account the source mechanism in the form of a double-couple. As the inversion time window extends from the direct P waves arrival to the S-wave coda, the site term is assumed to be similar for both P and S waves.

3.2.1 Monte Carlo simulations of seismogram envelopes

For a given source–receiver pair, $G_{ij}(t, f_0, \mu_S, \mu_S^*, \mu_S^a)$ is calculated using the Monte Carlo approach (Heller *et al.* 2022), which is commonly used to solve the radiative transfer equations (Gusev & Abubakirov 1987; Hoshiba 1994; Margerin *et al.* 2000; Lacombe *et al.* 2003; Przybilla *et al.* 2009). For each Monte Carlo simulation, 5 million phonons (or energy particles) are emitted at a point

source and perform a random walk in the medium. To build energy envelopes, we discretize the medium into cylindrical shells of radius and thickness both equal to 10 km and count the number of phonons present in each elementary volume at regular time intervals of 1 s (see Heller *et al.* 2022, for further details). We place a double-couple source at a depth of 1 km for the Le Teil earthquake and 9 km for the Lourdes earthquake, respectively. Fault parameters are set as follows: strike $= 62^\circ$, dip $= 59^\circ$ and rake $= 107^\circ$ for the Le Teil earthquake according to the CEA-LDG (http://www-dase.cea.fr/actu/dossiers_scientifiques/2019-11-11/index.html, last accessed: July 2023) and strike $= 115^\circ$, dip $= 60^\circ$ and rake $= -69^\circ$ for the Lourdes earthquake according to the Midi-Pyrénées Observatory (Mazzotti *et al.* 2021). Due to the shallow depth of the Le Teil earthquake, we expect an important excitation of surface waves at low frequency (see Figs 1d and S1–S6), which cannot yet be modelled in our Monte Carlo simulations. Although some progress has been made to include surface waves in envelope simulations (Xu *et al.* 2021), significant theoretical developments are still necessary to properly take into account coupling between surface and body waves in the radiative transfer modelling. The Moho depth H is set at 30 km for all the selected stations for the Le Teil earthquake and the stations MONQ and TERF for the Lourdes earthquake. H is set at 40 km for the station PC25 located in the Spanish Pyrenees. Due to the existence of a discontinuity in the Moho along the Northern Pyrenean fault (e.g. Chevrot *et al.* 2018), we tested different Moho depths for three stations (ATE, PC15 and MLS) with $H = 30$, 40 and 50 km. Eventually, we selected the depth providing the lowest misfit between data and synthetic envelopes as explained in the next section. For each source-station pair, we adjust the crustal velocity model (α and β) to match the onset of the direct arrivals. This step is important as small time shifts may result in biases in the estimation of scattering properties. Depending on the source-station path, crustal velocities are $5.41 \leq \alpha \leq 6.09$ km s^{-1} and $3.16 \leq \beta \leq 3.61$ km s^{-1}. In the mantle, P- and S-wave velocities are fixed at $\beta_m = 4.7$ km s^{-1} and $\alpha_m = \sqrt{3}\beta_m \approx 8.14$ km s^{-1}. Crustal and mantle densities are set to $\rho = 2.8$ and $\rho_m = 3.3$.

3.2.2 *Partial derivatives of seismogram envelopes*

In addition to the envelopes E^{ij}_{mod}, the partial derivatives with respect to the parameters μ_S and μ^a_S, also called sensitivity kernels, are computed. These kernels, which are needed for the optimization of μ_S and μ^a_S as discussed thereafter, are calculated by the differential Monte Carlo method (Takeuchi 2016). To facilitate the comparison between the scattering and absorption sensitivity kernels $\partial E/\partial \mu_S$, $\partial E/\partial \mu^a_S$, we plot these quantities on the same graph in Fig. 3 for epicentral distances fixed at 50, 150 and 250 km. Furthermore, we carefully distinguish between the P and S energy densities, although only the sum of the two is considered in the forward-modelling and the inversion. In Fig. 3, the time scale is normalized by the S wave mean free time $\tau_S = 1/\mu_S$ and the source is a unit energy double-couple with parameters corresponding to the Le Teil earthquake. The attenuation parameters are taken from the reference model of Lacombe *et al.* (2003) for France at 3 Hz ($l^*_S = l_S = 250$ km, $l^a_S = 150$ km). Note that to obtain smooth kernels such as those shown in Fig. 3, the number of simulated phonons needs to be significantly increased (5×10^9 in this case). In the Figure, we see that the scattering and absorption sensitivity kernels have similar magnitude in the time window between the direct P- and S-waves arrival times. It is worth noting that even in the P-coda, a large part of the sensitivity originates from converted shear waves. Efficient mechanisms for

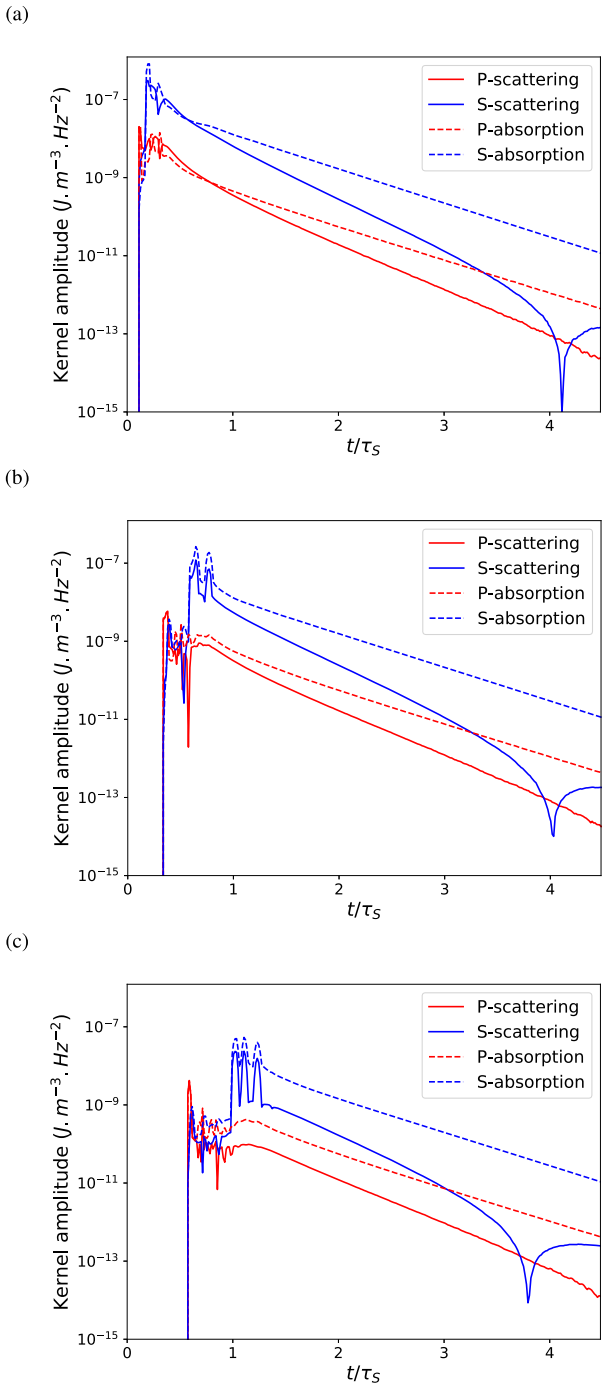

Figure 3. Absolute value of the partial derivatives of P- and S-energy envelopes with respect to the scattering (solid line) and absorption (dashed line) inverse times (μ_S, μ^a_S) as a function of time normalized by the S-wave mean free time. From top to bottom, epicentral distances are 50, 150 and 250 km (see text for other parameter settings).

such mode conversions are reflections at the free surface and scattering by small-scale heterogeneities in the vicinity of the receiver. Around the direct S waves, scattering and absorption affect the energy envelope equally, which is consistent with the well-known fact that the separation of attenuation mechanisms is impossible from analysis of direct waves only. The situation changes drastically in the S coda, where it can be observed that absorption largely dominates scattering. This in turn implies the important property that

the modelling of the complete seismogram envelope allows the separation of attenuation mechanisms. Roughly speaking, the direct *S*-wave constrains the total attenuation while the coda constrains the absorption. More exotic features can also be observed such as the decay of the *S*-wave scattering sensitivity kernel towards 0 visible between $t/\tau_S = 3.8$ and $t/\tau_S = 4.1$ in the coda (Fig. 3). At this lapse-time the scattering kernel changes sign (not visible in this figure). Such a sign inversion was previously pointed out by Mayor *et al.* (2014) in the scalar case. This property can be understood qualitatively as follows: increasing the scattering attenuation in the medium leads to a decrease of the coherent wave energy and therefore results in a negative sensitivity near the ballistic arrivals and in the early coda. By contrast, the energy backscattered at long lapse-time is increased. This is clear, for example, from the diffusion approximation whose amplitude scales like $(\mu_S^*)^{3/2}$. Therefore, we expect a positive sensitivity to scattering attenuation at long lapse-time.

In summary, we have argued that the time-dependent sensitivity of seismogram energy envelopes can be exploited to quantify the contributions of scattering and absorption from a single record. The separation procedure, which requires the joint modelling of direct arrivals and their coda is detailed hereafter.

3.3 Separation of source, attenuation and site parameters

Elaborating on previous works by Sens-Schönfelder & Wegler (2006); Eulenfeld & Wegler (2016); Eulenfeld *et al.* (2022), we developed an inversion procedure based on elastic radiative transfer theory to separate the source spectrum from attenuation and site parameters using seismogram records in the 0.375–24 Hz frequency band. The inversion procedure is divided into two steps: (1) invert the attenuation parameters μ_S, μ_S^*, μ_S^a or equivalently (l_S, l_S^a and l_S^*/l_S) and the product of the spectral source energy and site amplification $(WR)_{ij}$ for each source-station path from the selected data envelopes and (2) with a correct attenuation model, separate W_i from R_j. From the source energy, we in turn estimate the source displacement spectrum, then M_0 and M_w in the framework of a generalized Brune model (Brune 1970; Abercrombie 1995).

3.3.1 *Inversion of attenuation parameters*

As outlined in Section 3.1.3, three parameters suffice to completely specify the attenuation properties of the crust at a given frequency: μ_S, the coherent wave attenuation, μ_S/μ_S^* the scattering anisotropy parameter, and μ_S^a the anelastic attenuation. Despite the small number of unknowns, the solution of the inverse problem poses some difficulties. In particular, while scattering anisotropy is an important ingredient to model seismogram envelopes (e.g. Gusev & Abubakirov 1987; Sato 1989; Hoshiba 1995; Jing *et al.* 2014), several authors have pointed out the difficulty of resolving this parameter in inverse problems. Gaebler *et al.* (2015) used elastic radiative transfer theory to estimate scattering and absorption from observed seismogram envelopes and found that while l_S^* is generally well constrained, the anisotropy parameter l_S^*/l_S is poorly resolved by the data. Similar conclusions were reached by Calvet *et al.* (2023) in the framework of MLTWA inversions in the case where forward-scattering dominates. We recall that MLTWA (multiple lapse time window analysis, see Fehler *et al.* 1992) is a method to estimate attenuation based on radiative transfer theory. It allows the separation of scattering and absorption from the measurement of energy integrals of direct *S* wave and its coda in three consecutive time windows (+ a late normalization window). The conclusions of Calvet *et al.* (2023) are therefore relevant to our work. In other approaches such as peak delay time tomography (e.g. Takahashi *et al.* 2009), the scattering strength/scattering anisotropy trade-off is reflected in the fact that one usually seeks to retrieve the parameter ϵ^2/l_c only.

In the light of these observations, we complete step (1) by using a hybrid inversion approach which combines a grid-search for the scattering anisotropy (μ_S/μ_S^*) with an iterative optimization for μ_S, μ_S^a and $(WR)_{ij}$. For the later we use the Levenberg–Marquardt algorithm as implemented in the GNU Scientific Library (Galassi *et al.* 2002). Following Gaebler *et al.* (2015), the agreement between modelled envelopes and data is quantified by the χ^2 misfit function, defined as the least-squares difference between the logarithms of the normalized simulated energy envelopes $(WR)_{ij}G_{ij}(t_n, f_0)$ and the data envelopes $E_\mathrm{obs}^{ij}(t_n, f_0)$:

$$\chi^2 = \frac{1}{N}\sum_{n=1}^{N}\left(\log_{10}\left(E_\mathrm{obs}^{ij}(t_n, f_0)\right) - \log_{10}\left((WR)_{ij}(f_0)G_{ij}(t_n, f_0)\right)\right)^2. \tag{9}$$

In eq. (9), t_n denotes the sampling time of the envelopes and the sum is carried over the total number of samples N. In practice, we cut the records when the signal-to-noise ratio (defined in energy) decreases below 4. The time window for noise estimation is set before the signal onset and typically lasts several tens of seconds, dependent on the recording. Note that two smoothing operations are applied to simulated $G_{ij}(t_n, f_0)$ before computing the misfit χ^2. (1) A moving average window with the same duration as the one applied to data envelopes. (2) To take into account the temporal spreading of the signal energy due to the bandpass filtering of the waveforms, the synthetic envelopes are convolved with the normalized energy envelope of the impulse response of the filter. Note that to reduce the computational effort, the synthetic envelopes are azimuthally averaged. Such a simplification is supported by theoretical and observational studies showing that the focal mechanism is rapidly averaged out at high-frequency as a consequence of crustal scattering (Takemura *et al.* 2016). For stations located close to the epicentre (ADHE and PC15, see Fig. 1), we verify that the azimuthal average has no influence on the results (see Fig. S7). We also stress that the logarithm appearing in the definition of the misfit function is important to give similar weights to the ballistic and coda parts of the signals in the inversion process.

In practice, the method works as follows. For each source-station pair (i, j) and central frequency f_0, the grid-search algorithm is used to explore different levels of scattering anisotropy ranging from non-preferential to strongly forward-peaked ($\mu_S/\mu_S^* \in \{1, 2, 5, 10, 20, 40\}$). We note that there exists a one-to-one correspondence between l_c/λ and μ_S/μ_S^*. For each value of μ_S/μ_S^*, the Levenberg–Marquardt algorithm is used to jointly optimize μ_S, μ_S^a and $(WR)_{ij}$. This step uses the sensitivity kernels introduced in Section 3.2.2 to guide each iteration of the optimization process. Such an approach has already been successfully applied to envelope inversions of impacts and quake data on Mars (Menina *et al.* 2021, 2023). In the vast majority of cases, we find that the algorithm converges in a few steps towards a minimum which shows little dependence to the starting model, which indicates that once the scattering mechanism is fixed, the inverse problem for μ_S and μ_S^a has a unique solution (Fehler *et al.* 1992).

3.3.2 *Extraction of source parameters*

Once the propagation and energy terms $G_{ij}(t, f_0, l_S, l_S^*, l_S^a)$ and $(WR)_{ij}$ have been determined for each source-station pair and each

frequency, we proceed to the separation of the source and site terms, $W_i(f_0)$ and $R_j(f_0)$ in eq. (8). As the notations suggest, we assume that $W_i(f_0)$ is common to all seismogram records whereas $R_j(f_0)$ is specific to each station. We chose to extract the relative site effects with respect to the whole set of inverted stations. For this purpose, we assume that the logarithmic average of site amplifications over the network is equal to 0 (Sens-Schönfelder & Wegler 2006):

$$\left\langle \log\left(W_i(f_0)R_j(f_0)\right)\right\rangle = \log\left(W_i(f_0)\right), \tag{10}$$

where the brackets denote the average over all the selected stations.

For a double couple, the source spectral energy $W_i(\omega)$ is equal to the sum of the P- and S-wave spectra $W_i^P(\omega)$ and $W_i^S(\omega)$. $W_i(\omega)$ may be expressed as follows (Sato *et al.* 2012, p. 188):

$$W_i(\omega) = W_i^P(\omega) + W_i^S(\omega) = \frac{\omega^4\left|\hat{M}(\omega)\right|^2}{15\pi\rho\alpha^5} + \frac{\omega^4\left|\hat{M}(\omega)\right|^2}{10\pi\rho\beta^5}. \tag{11}$$

$\hat{M}(\omega)$ designates the Fourier transform of the seismic moment time function and $\omega = 2\pi f$. From eq. (11), we deduce the source displacement spectrum $\omega|\hat{M}(\omega)|$:

$$\omega\left|\hat{M}(\omega)\right| = \sqrt{\frac{W_i(\omega)}{\omega^2}\frac{30\pi\rho\beta^5\alpha^5}{2\beta^5+3\alpha^5}}, \tag{12}$$

Having estimated the source displacement spectrum, key parameters characterizing the source size can be calculated. By applying the source model developed by Abercrombie (1995), the seismic moment M_0 (expressed in N.m) can be related to the source displacement spectrum as follows:

$$\omega\left|\hat{M}(\omega)\right| = \frac{M_0}{\left(1+\left(\frac{f}{f_c}\right)^{\gamma n}\right)^{1/\gamma}}, \tag{13}$$

where f_c denotes the corner frequency, n the high-frequency spectral falloff exponent and γ an additional exponent controlling the shape of the transition between the low-frequency plateau of the spectrum at M_0 and its decaying part in f^{-n}. In the case where $n = 2$ and $\gamma = 1$ in eq. (13), the classical Brune source model is recovered (Brune 1970). M_0, f_c, n and γ can be estimated simultaneously by applying a non-linear least-square regression to the logarithm of the source displacement spectrum. For this purpose, eq. (13) can be rearranged in the following way:

$$\ln\left(\omega\left|\hat{M}(\omega)\right|\right) = \ln M_0 - \frac{1}{\gamma}\ln\left(1+\left(\frac{f}{f_c}\right)^{\gamma n}\right). \tag{14}$$

Eq. (14) is still too detailed for our purposes. In practice, we found it difficult to simultaneously resolve the exponents γ and n from the data. Since our main goal is to estimate M_0, we opted for a generalized Brune model by setting $\gamma = 1$. Finally, we convert the seismic moment M_0 to the moment magnitude M_w using the relationship given by Hanks & Kanamori (1979):

$$M_w = \frac{2}{3}\log_{10}(M_0) - 6.07. \tag{15}$$

In addition, from the parameters M_0 and f_c, it is possible to determine additional physical quantities characterizing the source such as the stress-drop $\Delta\sigma$, which can be expressed as:

$$\Delta\sigma = \frac{7}{16}M_0\left(\frac{f_c}{k\beta}\right)^3, \tag{16}$$

with $k = 0.37$ (Brune 1970). The inversion results are discussed hereafter.

4 RESULTS

4.1 Envelope modelling

The inversion procedure developed in Section 3 has been applied to the data set presented in Section 2. Synthetic envelopes $E^{ij}_{\rm mod}(t, f_0)$ are compared to data envelopes $E^{ij}_{\rm obs}(t, f_0)$ in Fig. 4 for the six records from the Le Teil (2019) event and in Fig. 5 for the six records from the Lourdes (2014) event, in a frequency band centred around $f_0 = 3$ Hz. Envelope fitting at other frequency bands between 0.375 and 24 Hz are shown in supplementary materials (Figs S8–S14). The synthetic envelopes shown here are those obtained with the scattering anisotropy (quantified by l_S^*/l_S) minimizing the cost function χ^2 (see eq. 9). We note that all observed envelopes are relatively well modelled from direct arrivals to the end of the S-wave coda. Small discrepancies between synthetics and data are nevertheless visible, mainly in the time window of the direct P wave and its coda. Depending on the station and the frequency, P-wave amplitudes may be either overestimated or underestimated. In the case of station ADHE, which is located in the vicinity of the epicentre of the Le Teil earthquake, direct arrivals may be more sensitive to attenuation properties in the upper crust and the S-wave coda sensitive to attenuation properties in the whole crust which may explain the relatively poor fit to the data since we assume uniform attenuation properties for the whole crust. As discussed in Wang & Shearer (2017), a crustal attenuation stratification may provide a better fit, but such an implementation is out of the scope of this study.

Furthermore, at low frequency ($\leq$1.5 Hz) we remark that the beginning of the S-wave coda is poorly modelled in the case of the Le Teil earthquake. This is illustrated in Fig. 6, where we compare best-fitting synthetics and data envelopes at central frequency $f_0 =$ 0.75 Hz for the Le Teil earthquake. The excess energy following the S-wave pulse and which is not explained by our model could be related to the excitation of surface waves since the hypocentre of this event is relatively shallow (about 1 km, e.g. Delouis *et al.* 2021). Apart from these issues, we found that the Levenberg–Marquardt algorithm converges to a model that satisfactorily explains the data in usually less than 10 iterations.

In Fig. 7, we illustrate the effect of scattering anisotropy on the fidelity of envelope modelling. An example of envelope fitting for the Le Teil earthquake at station LAJAS is shown in Fig. 7 a with the anisotropy parameter $l_S^*/l_S = 40$, providing the best fit to the data. For comparison, in Fig. 7 b we show the best-fitting envelope, assuming a non-preferential scattering mechanism ($l_S^*/l_S = 1$). It is apparent that non-preferential scattering provides a poorer fit to the data. In particular, this model predicts a direct S-wave arrival which is too impulsive and reproduces less accurately the overall shape of the S-wave envelope. Quantitatively, we find that the misfit χ^2 is higher by 67.7 per cent for $l_S^*/l_S = 1$ than for $l_S^*/l_S = 40$. The latter value corresponds to a strongly forward-peaked scattering mechanism. In such a case, the applicability of the Born approximation underlying transport theory may be questioned. To confirm the validity of our approach, we verified that the condition $\epsilon^2 l_c k_S^2 \ll 1$ with $k_S = 2\pi f_0/\beta$ was satisfied for all the best-fitting models of heterogeneity (Ryzhik *et al.* 1996).

We remark that the level of scattering anisotropy can have a large impact on the estimated scattering attenuation. In the case illustrated

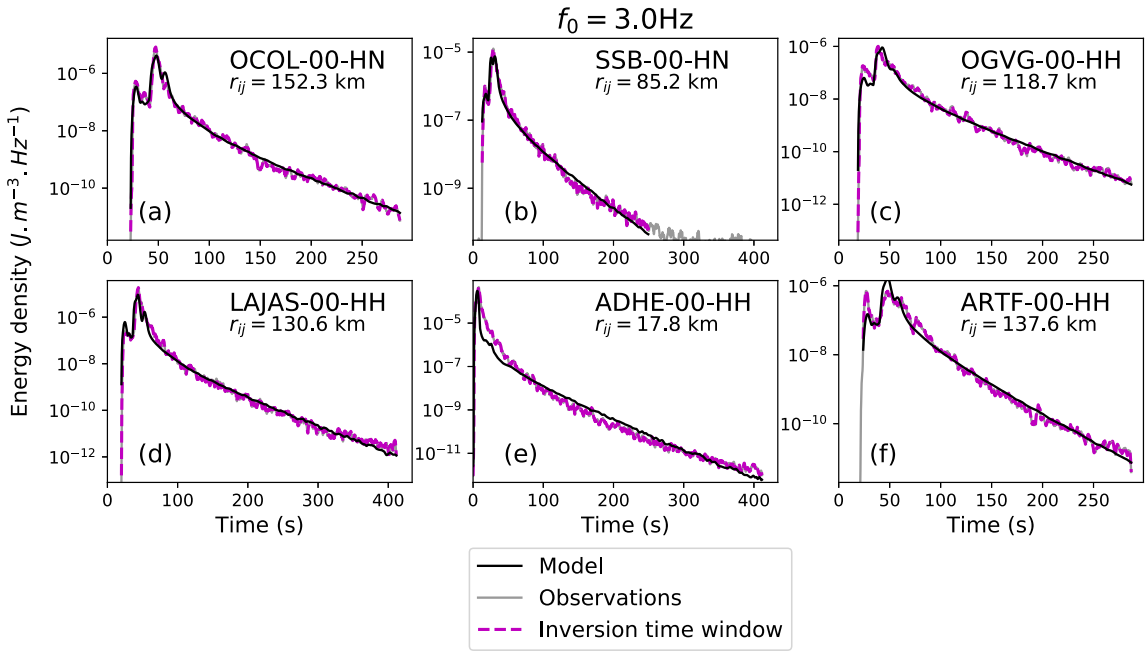

Figure 4. Comparison between best-fitting synthetic envelopes (solid black line) and data envelopes (magenta dashed line) at central frequency $f_0 = 3.0$ Hz for the Le Teil (2019) event. Epicentral distances are indicated in inset below the station code.

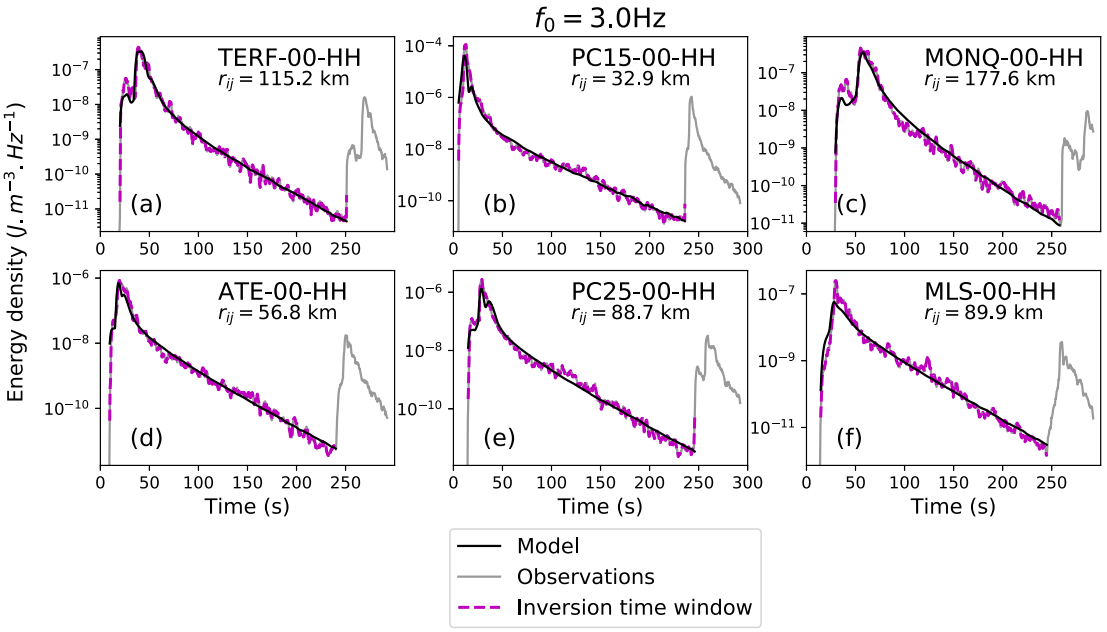

Figure 5. Comparison between best-fitting synthetic envelopes (solid black line) and data envelopes (magenta dashed line) at central frequency $f_0 = 3.0$ Hz for the Lourdes (2014) event. Epicentral distances are indicated in inset below the station code.

in Fig. 7, we find that when the anisotropy parameter increases from $l_S^*/l_S = 1$ to $l_S^*/l_S = 40$, l_S^* decreases from 1397 to 498 km. By contrast, l_S^a only increases from 135 to 166 km. This example indicates that a more accurate estimation of scattering attenuation can be expected from radiative transfer models that incorporate the effect of scattering anisotropy compared to purely isotropic models. For most stations, we verify that the anisotropic model improves the data fitting (see Fig. S15). Globally we observe that a low-to-moderate forward scattering model ($l_S^*/l_S \approx 1 - 10$) at low frequency ($f_0 \leq$ 0.75 Hz) and a very forward scattering model ($l_S^*/l_S > 10$) at higher frequency better explain data envelopes. Overall, our results show that iterative linearized envelope inversion based on radiative transfer theory is feasible for polarized elastic waves in a crustal waveguide. This approach allows an estimation of the average crustal scattering and absorption properties and provides a satisfactory model for the high-frequency propagation term. In the next section, we examine in more details the variability of attenuation parameters inferred from envelope inversion.

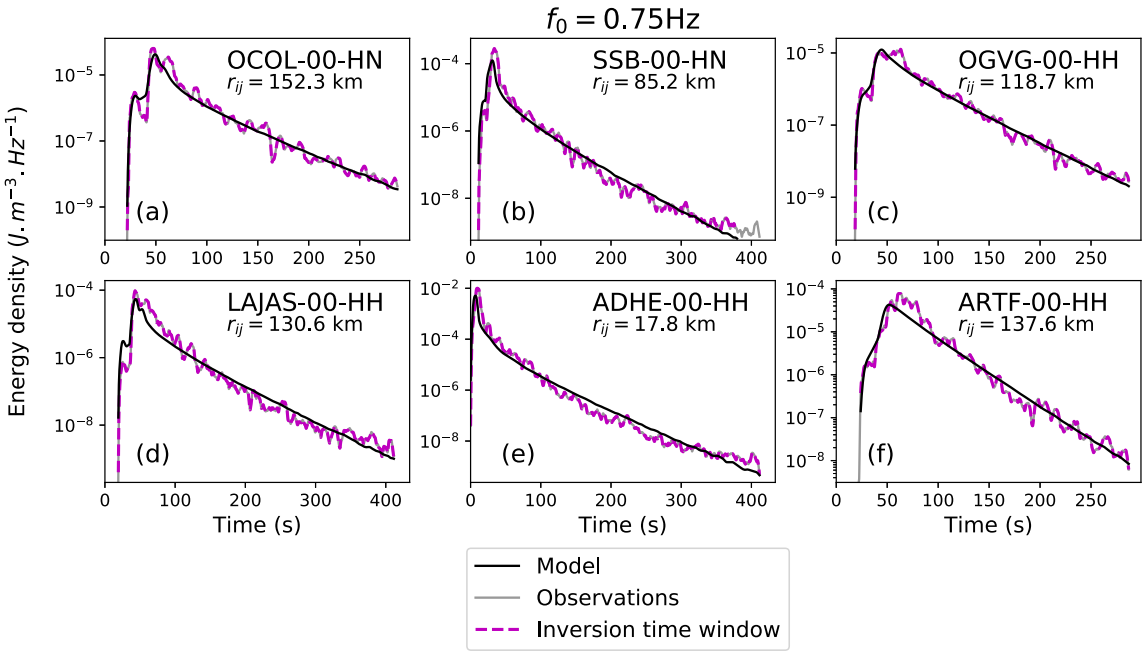

Figure 6. Comparison between best-fitting synthetic envelopes (solid black line) and data envelopes (magenta dashed line) at central frequency $f_0 = 0.75$ Hz for the Le Teil (2019) event. Epicentral distances are indicated in inset below the station code.

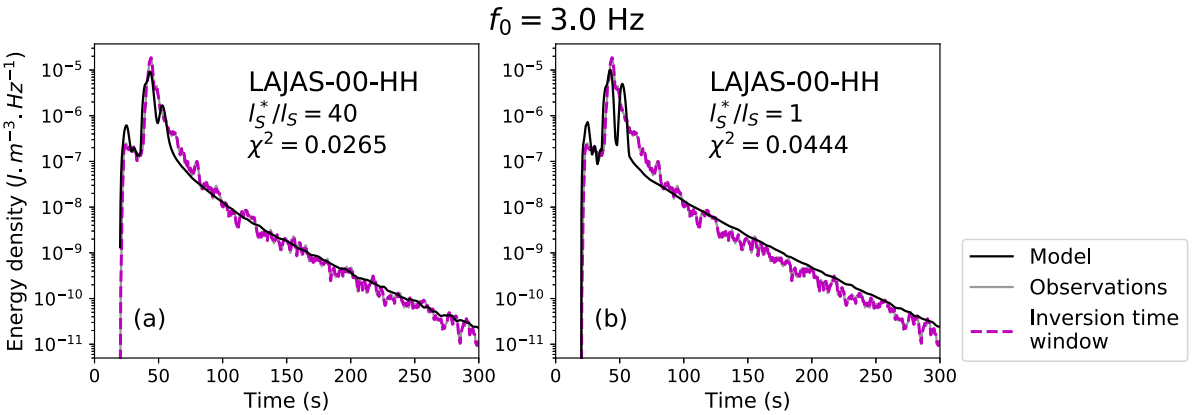

Figure 7. (a) Comparison between best-fitting synthetic envelopes (solid black line) and data envelopes (magenta dashed line) at central frequency $f_0 = 3.0$ Hz for the Le Teil (2019) event recorded at the station LAJAS in the Southern Central Massif. (b) Same but a non-preferential scattering ($l_S^*/l_S = 1$) is assumed.

4.2 Attenuation parameters

4.2.1 General description

Fig. 8 shows the frequency-dependent attenuation parameters $\left({}^{S}Q_{sc}^{*}\right)^{-1}$ and $({}^{S}Q_i)^{-1}$ inverted for each source-station pair in the case of the Le Teil and Lourdes earthquakes. The corresponding transport mean free paths and absorption lengths (as well as the scattering/absorption quality factors) with their uncertainties are reported in Tables 1 and 2, respectively. In addition, we provide the values of the best-fitting anisotropy parameter l_S^*/l_S and the minima of the misfit function. Comparing the attenuation curves in Fig. 8, we observe a significant variability of the attenuation parameters depending on the frequency and the source-station path. Before delving into the details, we provide general comments on the frequency dependence of attenuation.

To facilitate the comparison with other studies, we summarize our attenuation measurements with a power law ($Q = Q_0 f^{\eta}$) for absorption and scattering quality factors of S waves defined in eq. (5). In each region, we determined Q_0 and η from a linear least-square fit of the logarithm of the median of the inverse quality factors $\left({}^{S}Q_{sc}^{*}\right)^{-1}$ and $({}^{S}Q_i)^{-1}$ over the 6 inverted stations. For the region corresponding to the Le Teil (2019) ans Lourdes (2014) earthquakes, we find ${}^{S}Q_i = 378 f^{0.64}$, ${}^{S}Q_{sc}^{*} = 283 f^{1.26}$ and ${}^{S}Q_i = 361 f^{0.64}$, ${}^{S}Q_{sc}^{*} = 252 f^{1.13}$, respectively. To aid the comparison with studies that only provide estimates of apparent attenuation, we also determine the power law for the total (or extinction) quality factors (eq. 6). We find ${}^{S}Q_e = 160 f^{0.88}$ and ${}^{S}Q_e = 148 f^{0.83}$ for the Le Teil and Lourdes regions, respectively. The range of determined power-law exponents in France is typical of the values reported in the literature for the total attenuation (see Sato *et al.* 2012, chapter 5). Perhaps more interestingly, our study highlights the distinct frequency behaviour of scattering versus absorption, with an exponent η about twice larger for the former than the latter. The values of these exponents put critical constraints on the possible mechanisms at the origin of attenuation. On average, the seismic albedo (i.e. the

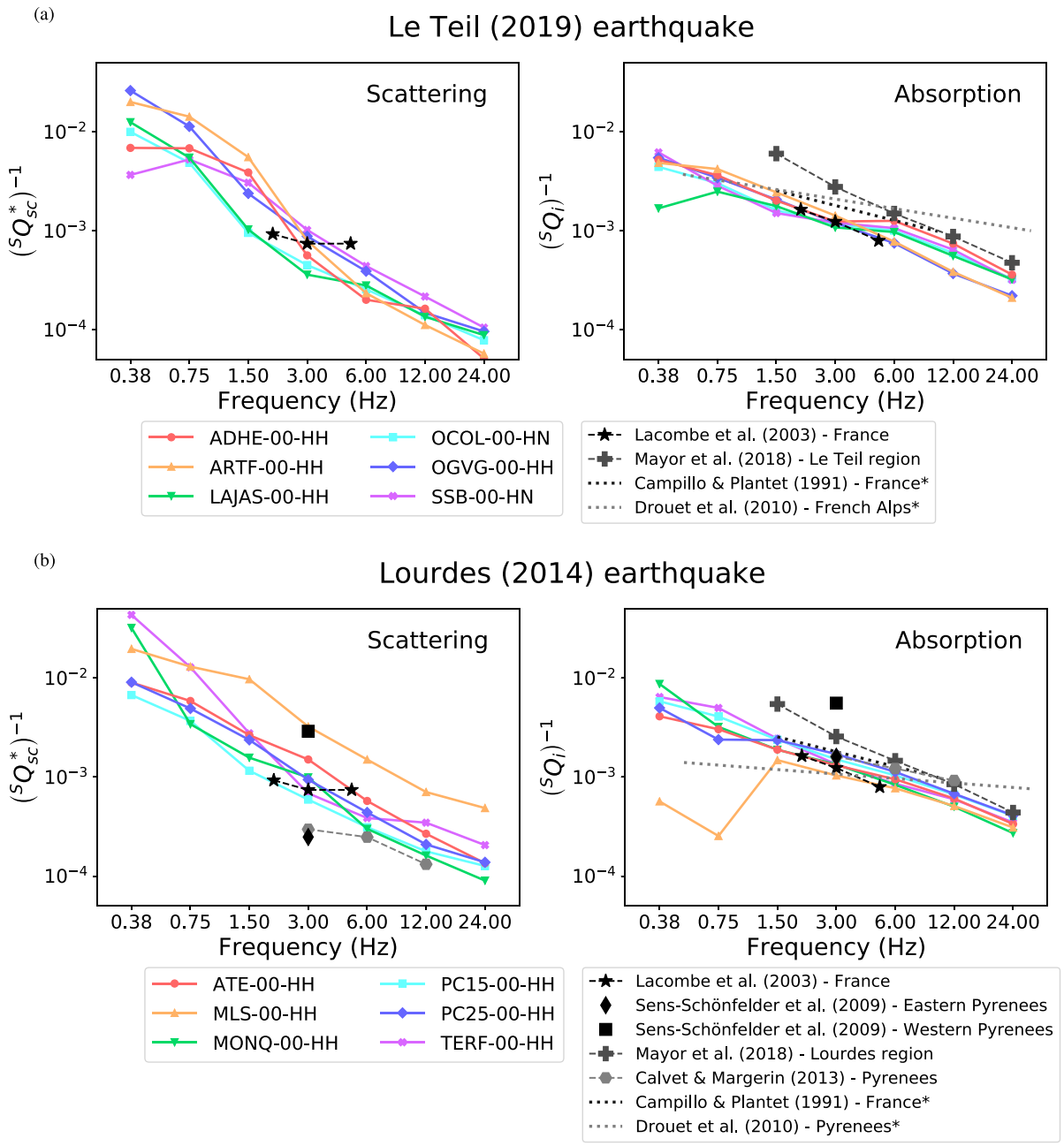

Figure 8. Attenuation parameters $\left({}^{S}Q^{*}_{sc}\right)^{-1}$ and $({}^{S}Q_{i})^{-1}$ as a function of frequency for the Le Teil (a) and Lourdes earthquakes (b). The reported values correspond to the scattering mechanism providing the lowest misfit, which may change with frequency. Comparison with other studies is shown in grey and black. In the studies marked with an asterisk, total attenuation is retrieved from direct *S* or *Lg* waves.

fraction of attenuation caused by scattering) decreases approximately like $f^{-0.32}$ with absorption dominating scattering for frequencies typically greater than 1.5–3 Hz. This trend is generally in line with what has been found in different regions of the world (Sato *et al.* 2012).

Looking at our attenuation estimates in more details, it is clear from Fig. 8 that scattering shows greater intraregional variability than absorption. Quantitatively, for a fixed frequency band, scattering typically varies by a factor of 3–5 depending on the source-station path, while absorption varies by a factor of only 1.5–2. This observation must be counter-balanced by analysing the uncertainties in attenuation parameters reported in Tables 1 and 2. Indeed, we remark that they are significantly larger for scattering than absorption. Looking at the sensitivity kernels in Fig. 3, we remark that envelopes are mostly sensitive to scattering near ballistic arrivals, which correspond to only a small fraction of the inversion time window. In addition, we note that direct waves are subject to large variability in amplitude due to the source mechanism. By contrast, absorption affects the envelope in the whole inversion time window, suggesting that this quantity is better constrained.

In the region of the Le Teil earthquake (Fig. 8a), absorption in the Central Massif (stations OCOL and LAJAS) is weaker than in the Alps (stations ARTF and OGVG) at low frequency, a pattern that reverses at high frequency. In the Pyrenees (Fig. 8b), $({}^{S}Q_{i})^{-1}$

Table 1. Inverted attenuation parameters [lengths l_S^* and l_S^a, quality factors (eq. 5), best model misfit χ^2 and the corresponding value of l_S^*/l_S minimizing χ^2] for the Le Teil (2019) earthquake, as a function of frequency. All uncertainties correspond to the 95 per cent confidence interval.

Station name	f_0 (Hz)	l_S^* (km)	l_S^a (km)	${}^S Q_{sc}^*$	${}^S Q_i$	l_S^*/l_S	χ^2
	0.375	148.62 ± 29.34	335.79 ± 10.95	100.02 ± 19.74	225.99 ± 7.37	10	0.0246
	0.75	152.53 ± 30.39	244.92 ± 6.95	205.31 ± 40.90	329.67 ± 9.35	10	0.0289
	1.5	389.53 ± 74.53	230.06 ± 6.24	1048.62 ± 200.65	619.32 ± 16.79	40	0.0207
OCOL-00-HN	3.0	412.35 ± 79.35	158.79 ± 3.82	2220.08 ± 427.23	854.93 ± 20.57	40	0.0253
	6.0	361.99 ± 66.56	92.34 ± 1.15	3897.89 ± 716.67	994.31 ± 12.41	40	0.0169
	12.0	331.03 ± 60.28	77.78 ± 0.80	7129.12 ± 1298.24	1675.11 ± 17.17	40	0.0149
	24.0	295.42 ± 52.41	70.88 ± 0.74	12724.48 ± 2257.38	3052.76 ± 31.81	40	0.0107
	0.375	402.18 ± 48.35	238.08 ± 4.23	272.32 ± 32.74	161.21 ± 2.87	1	0.0141
	0.75	140.43 ± 16.33	258.54 ± 6.16	190.18 ± 22.12	350.12 ± 8.34	2	0.0308
	1.5	120.53 ± 14.15	244.12 ± 4.32	326.44 ± 38.32	661.18 ± 11.69	5	0.0185
SSB-00-HN	3.0	180.75 ± 22.28	152.86 ± 1.43	979.09 ± 120.69	828.05 ± 7.74	40	0.0081
	6.0	209.17 ± 26.39	86.62 ± 0.72	2266.11 ± 285.89	938.45 ± 7.75	40	0.0082
	12.0	212.70 ± 24.40	71.51 ± 0.39	4608.73 ± 528.77	1549.55 ± 8.46	40	0.0105
	24.0	218.75 ± 28.17	72.15 ± 0.74	9479.45 ± 1220.84	3126.59 ± 32.10	40	0.0083
	0.375	52.88 ± 10.06	251.84 ± 9.76	38.32 ± 7.29	182.48 ± 7.07	2	0.0151
	0.75	60.87 ± 11.11	200.88 ± 5.88	88.21 ± 16.10	291.10 ± 8.52	5	0.0143
	1.5	144.56 ± 28.66	166.64 ± 3.56	418.97 ± 83.05	482.95 ± 10.31	20	0.0254
OGVG-00-HH	3.0	195.71 ± 37.83	143.57 ± 2.89	1134.43 ± 219.30	832.19 ± 16.73	40	0.0308
	6.0	220.52 ± 41.21	114.62 ± 2.32	2556.44 ± 477.78	1328.76 ± 26.88	40	0.0459
	12.0	289.89 ± 54.16	116.47 ± 2.65	6721.44 ± 1255.81	2700.41 ± 61.36	40	0.0433
	24.0	223.72 ± 42.12	97.49 ± 1.63	10374.40 ± 1953.34	4520.76 ± 75.73	20	0.0326
	0.375	115.06 ± 16.13	852.56 ± 30.13	79.94 ± 11.21	592.37 ± 20.93	5	0.0112
	0.75	131.06 ± 18.63	288.95 ± 6.59	182.12 ± 25.89	401.53 ± 9.15	2	0.0354
	1.5	348.23 ± 48.17	202.47 ± 2.69	967.84 ± 133.88	562.70 ± 7.47	5	0.0335
LAJAS-00-HH	3.0	498.22 ± 69.71	166.24 ± 2.65	2769.35 ± 387.48	924.06 ± 14.75	40	0.0265
	6.0	320.39 ± 43.69	92.47 ± 0.82	3561.77 ± 485.70	1027.97 ± 9.15	40	0.0087
	12.0	331.33 ± 44.86	80.52 ± 0.74	7366.93 ± 997.37	1790.26 ± 16.47	40	0.0109
	24.0	254.28 ± 34.05	69.60 ± 0.50	11307.16 ± 1513.93	3095.07 ± 22.36	40	0.0091
	0.375	199.90 ± 14.39	263.79 ± 3.51	145.28 ± 10.46	191.71 ± 2.55	2	0.0081
	0.75	100.85 ± 7.09	189.02 ± 2.20	146.59 ± 10.30	274.74 ± 3.20	1	0.0460
	1.5	88.44 ± 6.27	170.18 ± 1.97	257.10 ± 18.22	494.72 ± 5.71	1	0.0617
ADHE-00-HH	3.0	304.36 ± 23.13	138.45 ± 1.15	1769.59 ± 134.46	804.93 ± 6.67	10	0.0598
	6.0	427.23 ± 31.52	68.15 ± 0.29	4967.95 ± 366.54	792.46 ± 3.33	1	0.0255
	12.0	262.95 ± 19.90	57.85 ± 0.24	6115.20 ± 462.77	1345.47 ± 5.59	20	0.0263
	24.0	419.16 ± 39.17	59.49 ± 0.41	19496.37 ± 1822.09	2766.98 ± 19.13	20	0.0186
	0.375	68.59 ± 12.34	282.82 ± 10.68	49.93 ± 8.98	205.88 ± 7.77	5	0.0213
	0.75	48.26 ± 6.47	163.11 ± 4.19	70.27 ± 9.43	237.47 ± 6.10	5	0.0207
	1.5	61.84 ± 10.73	140.26 ± 2.85	180.07 ± 31.26	408.41 ± 8.31	5	0.0241
ARTF-00-HH	3.0	215.65 ± 43.42	120.46 ± 2.19	1255.82 ± 252.85	701.52 ± 12.77	20	0.0200
	6.0	365.93 ± 70.83	110.20 ± 2.46	4262.02 ± 824.91	1283.48 ± 28.70	40	0.0341
	12.0	383.41 ± 74.90	111.40 ± 2.61	8931.26 ± 1744.71	2594.97 ± 60.79	40	0.0515
	24.0	373.07 ± 74.03	101.80 ± 2.01	17380.48 ± 3448.87	4742.92 ± 93.82	10	0.0439

decreases in a similar way at stations TERF, ATE, PC15 and PC25 for frequencies larger than 1.5 Hz. Large variability of absorption properties is visible at the lowest frequency (0.375 Hz). In particular, anomalously weak absorption is found at station MLS. We could not determine whether this feature is real or an artefact related to the competition between energy leakage and absorption in modelling the coda decay.

In the region of the Le Teil earthquake, scattering is generally more pronounced at stations located in the Alps than at those located in the Central Massif at low frequency (≤3 Hz; Fig. 8a). At high frequency (≥6 Hz), little variability is observed among the different stations. In the region of the Lourdes earthquake, patterns of scattering attenuation that deviate from the general trend are observed at stations MONQ and TERF in the Aquitaine Basin. Stations PC15, PC25, ATE and MLS in the central Pyrenees show similar frequency dependence with three times larger attenuation at MLS than at other stations at all frequencies.

Owing to the grid-search exploration, we find that a moderately forward scattering mechanism best explains the data at low frequency ($l_S^*/l_S \approx 1 - 10$ for $f_0 \leq 0.75$ Hz). By contrast, strong forward scattering is the preferred mechanism to explain high-frequency data, with l_S^*/l_S reaching the value of 40—the largest explored—in most cases for $f_0 \geq 3$ Hz (see Tables 1 and 2). This result is consistent with independent studies carried out in different regions of Europe (e.g. Przybilla *et al.* 2009; Calvet *et al.* 2013; Gaebler *et al.* 2015). Nevertheless, we remark that a broad range of l_S^*/l_S can give similar misfits (see Fig. S15) which shows that the anisotropy parameter is poorly resolvable. For further discussions of the trade-off between scattering strength and anisotropy, we refer the reader to Gaebler *et al.* (2015) or Calvet *et al.* (2023).

Table 2. Inverted attenuation parameters (lengths l_S^* and l_S^a, quality factors (eq. 5), best model misfit χ^2, and the corresponding value of l_S^*/l_S minimizing χ^2) for the Lourdes (2014) earthquake, as a function of frequency. All uncertainties correspond to the 95 per cent confidence interval.

Station name	f_0 (Hz)	l_S^* (km)	l_S^a (km)	${}^S Q_{sc}^*$	${}^S Q_i$	l_S^*/l_S	χ^2
	0.375	30.89 ± 4.41	208.49 ± 10.44	23.00 ± 3.29	155.20 ± 7.77	2	0.0219
	0.75	52.25 ± 10.04	134.46 ± 3.88	77.78 ± 14.95	200.19 ± 5.78	1	0.0218
	1.5	121.23 ± 26.18	137.64 ± 3.58	360.97 ± 77.95	409.84 ± 10.67	40	0.0198
TERF-00-HH	3.0	244.88 ± 52.32	124.59 ± 2.96	1458.27 ± 311.55	741.98 ± 17.64	40	0.0197
	6.0	217.55 ± 47.22	97.95 ± 1.76	2591.07 ± 562.40	1166.58 ± 20.94	40	0.0139
	12.0	121.16 ± 26.73	70.38 ± 0.99	2886.08 ± 636.69	1676.44 ± 23.64	40	0.0143
	24.0	102.06 ± 19.98	60.34 ± 0.80	4862.30 ± 951.93	2874.58 ± 38.05	40	0.0115
	0.375	198.96 ± 52.76	230.32 ± 8.97	148.30 ± 39.33	171.67 ± 6.68	40	0.0413
	0.75	181.63 ± 49.10	164.01 ± 5.65	270.77 ± 73.19	244.50 ± 8.42	40	0.0595
	1.5	289.29 ± 80.18	140.69 ± 3.73	862.52 ± 239.07	419.47 ± 11.11	40	0.0502
PC15-00-HH	3.0	283.09 ± 77.17	110.97 ± 2.36	1688.05 ± 460.14	661.74 ± 14.08	40	0.0428
	6.0	268.84 ± 70.05	80.57 ± 1.34	3206.20 ± 835.36	960.82 ± 15.99	40	0.0349
	12.0	235.75 ± 53.92	62.95 ± 0.94	5623.04 ± 1286.19	1501.37 ± 22.41	20	0.0646
	24.0	165.56 ± 38.28	51.62 ± 0.73	7897.68 ± 1826.05	2462.35 ± 34.74	40	0.0591
	0.375	45.14 ± 5.20	166.29 ± 5.32	31.10 ± 3.58	114.56 ± 3.66	2	0.0302
	0.75	211.71 ± 46.75	225.75 ± 7.37	291.71 ± 64.42	311.06 ± 10.16	5	0.0237
	1.5	230.99 ± 51.43	191.97 ± 5.37	636.54 ± 141.74	529.03 ± 14.81	40	0.0243
MONQ-00-HH	3.0	182.69 ± 41.01	135.08 ± 3.17	1006.88 ± 226.03	744.47 ± 17.48	40	0.0267
	6.0	302.38 ± 67.73	108.56 ± 2.26	3333.19 ± 746.64	1196.70 ± 24.91	40	0.0163
	12.0	280.99 ± 62.19	90.27 ± 1.53	6194.74 ± 1370.97	1990.15 ± 33.65	40	0.0207
	24.0	251.79 ± 53.67	83.42 ± 1.36	11102.10 ± 2366.29	3678.36 ± 59.77	40	0.0252
	0.375	150.25 ± 34.34	329.71 ± 21.29	110.83 ± 25.33	243.21 ± 15.70	2	0.0675
	0.75	115.43 ± 26.29	222.80 ± 9.63	170.29 ± 38.79	328.69 ± 14.20	5	0.0381
	1.5	127.68 ± 29.39	178.98 ± 6.28	376.72 ± 86.71	528.10 ± 18.52	10	0.0169
ATE-00-HH	3.0	112.50 ± 26.02	128.94 ± 3.45	663.84 ± 153.57	760.86 ± 20.36	5	0.0260
	6.0	147.54 ± 33.59	89.17 ± 1.65	1741.33 ± 396.44	1052.45 ± 19.42	20	0.0257
	12.0	158.18 ± 35.74	69.77 ± 1.02	3733.76 ± 843.58	1646.88 ± 24.05	40	0.0664
	24.0	156.81 ± 36.03	63.07 ± 0.84	7402.72 ± 1701.05	2977.42 ± 39.50	40	0.0907
	0.375	151.41 ± 31.61	275.22 ± 14.31	110.06 ± 22.98	200.06 ± 10.40	40	0.0165
	0.75	139.52 ± 29.45	287.53 ± 13.26	202.83 ± 42.82	418.03 ± 19.28	40	0.0283
	1.5	144.74 ± 30.94	145.58 ± 4.07	420.86 ± 89.95	423.29 ± 11.82	10	0.0141
PC25-00-HH	3.0	182.65 ± 38.62	100.64 ± 1.93	1062.18 ± 224.59	585.27 ± 11.25	20	0.0311
	6.0	195.43 ± 41.88	76.28 ± 1.21	2272.99 ± 487.07	887.15 ± 14.02	40	0.0215
	12.0	205.70 ± 40.28	63.31 ± 0.87	4784.79 ± 936.99	1472.69 ± 20.21	40	0.0318
	24.0	155.86 ± 24.99	52.42 ± 0.66	7251.12 ± 1162.81	2438.53 ± 30.59	40	0.0301
	0.375	77.77 ± 14.86	2699.06 ± 557.95	50.71 ± 9.69	1759.79 ± 363.78	5	0.0282
	0.75	58.75 ± 9.30	3016.93 ± 265.15	76.61 ± 12.13	3934.08 ± 345.75	40	0.0342
	1.5	39.39 ± 6.45	258.33 ± 10.67	102.73 ± 16.83	673.73 ± 27.84	10	0.0233
MLS-00-HH	3.0	59.19 ± 9.96	184.57 ± 5.28	308.72 ± 51.94	962.69 ± 27.53	40	0.0342
	6.0	63.75 ± 11.40	124.35 ± 2.55	665.07 ± 118.94	1297.24 ± 26.57	40	0.0293
	12.0	67.83 ± 12.02	93.85 ± 1.57	1415.21 ± 250.79	1958.06 ± 32.66	40	0.0398
	24.0	49.25 ± 8.17	77.45 ± 1.03	2055.12 ± 340.80	3231.87 ± 43.10	40	0.0414

4.2.2 *Comparison with other studies*

In the case of Metropolitan France, some attenuation estimates are available from the literature, which we now discuss. The studies by Lacombe *et al.* (2003), Sens-Schönfelder *et al.* (2009) and Calvet & Margerin (2013) are the most relevant to our work since these authors provide separate estimates for scattering and absorption based on radiative transfer theory. Lacombe *et al.* (2003) consider a waveguide geometry in the scalar approximation with isotropic scattering and analyse data from Central France. Their estimates for both scattering and absorption attenuation at 3 Hz ($1/{}^S Q_{sc}^* \approx 1.2 \times 10^{-3}$, $1/{}^S Q_i \approx 7.4 \times 10^{-4}$) are in excellent agreement with our findings for the Le Teil region.

Sens-Schönfelder *et al.* (2009) consider elastic radiative transfer theory in a waveguide geometry and focus particularly on the blockage of L_g waves in the western part of the Pyrenees. Their estimate for absorption in the Eastern part of the range agrees well with ours for the Lourdes region. By contrast, these authors report anomalously high absorption across the Labourd area which is delimited by strongly positive Bouguer and velocity anomalies (Vacher & Souriau 2001). The only path in our data set that grazes the Labourd anomaly is from Lourdes to ATE but it does not show particularly high $({}^S Q_i)^{-1}$. In the case of scattering attenuation, the estimate of Sens-Schönfelder *et al.* (2009) for the Eastern Pyrenees ($1/{}^S Q_{sc}^* \approx 2.5 \times 10^{-4}$) is about three to four times lower than ours, while the strong scattering attenuation in the western part of the range ($1/{}^S Q_{sc}^* \approx 2.9 \times 10^{-3}$) coincides with our finding at station MLS. It is worth noting that the Lourdes–MLS path crosses longitudinally the Saint–Gaudens area which, like the Labourd region, is characterized by strongly positive Bouguer and velocity anomalies (Vacher & Souriau 2001). In addition, we remark that scattering attenuation at station ATE, whose source-station path lies close to the Labourd anomaly, is two times larger in Sens-Schönfelder *et al.*

(2009) than in our study. This apparent discrepancy is most likely related to the very limited spatial extension of the Labourd anomaly.

Calvet & Margerin (2013) use scalar radiative transfer theory with non-isotropic scattering in a half-space geometry to model the lapse-time dependence of coda-Q at multiple frequencies in the Pyrenees. These authors generally find slightly weaker scattering attenuation and slightly stronger intrinsic attenuation than in our study. It is worth keeping in mind that the separation method of Calvet & Margerin (2013) is not based on the usual ratio between coherent and incoherent energies which, in addition to the much larger data set analysed by these authors, may partly explain the difference with our study.

Other studies that report estimates of the total apparent attenuation in France are worth mentioning. Campillo & Plantet (1991) estimated ${}^{Lg}Q = 320f^{0.50}$ for the apparent attenuation of L_g waves in the 1–10 Hz frequency band, which is in reasonable agreement with our findings for absorption. Mayor *et al.* (2018) performed an attenuation tomography for France based on the decay of the coda of S waves, taking into account their spatial sensitivity (Mayor *et al.* 2014). The average of their estimates of the coda quality factor over a radius of 150 km around the epicentre of the Le Teil earthquake yields $Q_c = 125f^{0.90}$ in the 1–32 Hz frequency bands. The frequency exponent is close to our estimate for total attenuation but suggests stronger attenuation than in our study. With $Q_c = 136f^{0.89}$ in the Lourdes region, the results of Mayor *et al.* (2018) are in rather good agreement with our findings for the total attenuation in this region. As a final point of comparison, we report the results of the generalized inversion by Drouet *et al.* (2010). For the Alps region, these authors determined ${}^{S}Q = 336f^{0.32}$ which differs quite significantly from our findings in the Le Teil region, particularly at high-frequency. The discrepancy is even more pronounced in the Pyrenees where Drouet *et al.* (2010) report (${}^{S}Q = 790f^{0.15}$) leading to an underestimation of attenuation at low-frequency and an overestimation at high-frequency. As pointed out by the authors, attenuation is the most difficult parameter to determine using generalized inversion all the more so as trade-offs between different parameters of the model are possible.

In the next section, we identify the site response using our envelope modelling method and compare the results with the classical coda normalization approach.

4.3 Site parameters

Site amplifications in energy $R_j(f_0)$ have been calculated using eq. (10). Note that there is no reference station in our approach, so that amplifications are measured with respect to the network average. In Fig. 9, we plot the frequency dependent site factors for each of the six selected stations from the Le Teil (Fig. 9a) and Lourdes (Fig. 9b) events. The results are compared with the site amplifications $R_j^{\text{coda}}(f_0)$ given by the coda normalization approach (Phillips & Aki 1986). We define $R_j^{\text{coda}}(f_0)$ as the ratio between the integrated energy in the coda recorded at station j and its average over all stations, calculated in a 20s time window starting 140s after the origin time. For our data set, this corresponds to a portion of the signal where all seismogram envelopes follow a common decay (in a given region). The site amplifications determined by each approach show good similarity, despite moderate differences that can reach a factor of 2 to 3, likely to be caused by the regional variations in attenuation properties highlighted in Section 4.2. Indeed, at most stations, we observe that differences in site amplification are correlated with attenuation along the source-station path. For instance, at station OCOL, attenuation (both scattering and absorption) is weak, which tends to increase the energy in the coda. This explains the larger site amplification found in our approach than the one predicted by the coda normalization method. On the contrary, in strong attenuation zones, for example at station ARTF, we determined a lower site amplification than the one predicted by the coda normalization approach. This shows that a path-dependent attenuation model is crucial to estimate site amplifications. This remark also applies to empirical approaches, as already proposed by Wang & Shearer (2019).

4.4 Source parameters

Fig. 10 shows the source displacement spectrum for the Le Teil and Lourdes earthquakes, obtained from eq. (12), in the 0.375–24 Hz frequency band. Raw spectra derived for each station, i.e. uncorrected from site amplifications, are also shown in the figure. For each event, the best-fitting source model given by eq. (13) with $\gamma = 1$ is superimposed on the inverted spectra. For the Le Teil earthquake, the linear regression (see eq. 14) yields $M_0 = 4.37 \pm 2.52.10^{16}$ N.m, $f_c = 0.72 \pm 0.26$ Hz and $n = 2.73 \pm 0.23$. Applying eq. (15), we determine a moment magnitude $M_w = 5.02 \pm 0.17$. All uncertainties correspond to the 95 per cent confidence interval. For the Lourdes earthquake, we obtain $M_0 = 2.31 \pm 1.19.10^{15}$ N.m, $f_c = 1.29 \pm 0.67$ Hz, $\gamma = 1.0$ (constrained), $n = 2.07 \pm 0.34$ and a moment magnitude $M_w = 4.17 \pm 0.15$.

The estimated magnitude M_w for the Le Teil earthquake is slightly higher than those determined by other independent studies, where M_w is typically found around 4.8–4.9 (e.g. Ritz *et al.* 2020; De Novellis *et al.* 2020; Causse *et al.* 2021; Delouis *et al.* 2021; Vallage *et al.* 2021). This overestimation may be caused by site effects which have not been fully removed, since amplifications are defined with respect to the network of stations selected for the inversion, rather than a reference station at a rock site. In the case of the Lourdes earthquake, the magnitude M_w estimated by our approach is in good agreement with the FMHex-20 database (Mazzotti *et al.* 2021) which reports $M_w = 4.2$. The later value has been determined from centroid-moment tensor inversions, using the method of Pondrelli *et al.* (2002).

We remark that the high-frequency fall-off of the source spectrum of the Lourdes earthquake ($n = 2.07$) is very close to the value $n = 2$ predicted by the Brune (1970) model. By contrast, in the case of the Le Teil earthquake, the exponent $n = 2.73$ implies that this event radiates less high frequency than expected from Brune's model. Significant departures from the omega-squared model have previously been reported in the literature for small-to-moderate earthquakes (Abercrombie 1995; Eulenfeld & Wegler 2016; Picozzi *et al.* 2017; Eken 2019). Such deviations maybe explained by the rupture process itself (e.g. Kaneko & Shearer 2014) or by the unusual depth of the fault rupture, of the order of 1 to 2 km (e.g. Delouis *et al.* 2021) with observable surface discontinuity in the Le Teil area. Indeed, for such a shallow source, the high-frequency radiation may be greatly attenuated by near-surface absorbing layers located in the vicinity of the epicentre. While neglected in our model, such a stratification of attenuation properties may be taken into account in future works.

In the case of the Lourdes earthquake, we remark that the source spectrum does not exhibit a clear plateau below the corner frequency. Several hypotheses may be invoked to explain this observation. The most trivial one is that the corner frequency is lower than can be determined from the data. This explanation is to be ruled out since we generally find an energy S/N of the order of 100

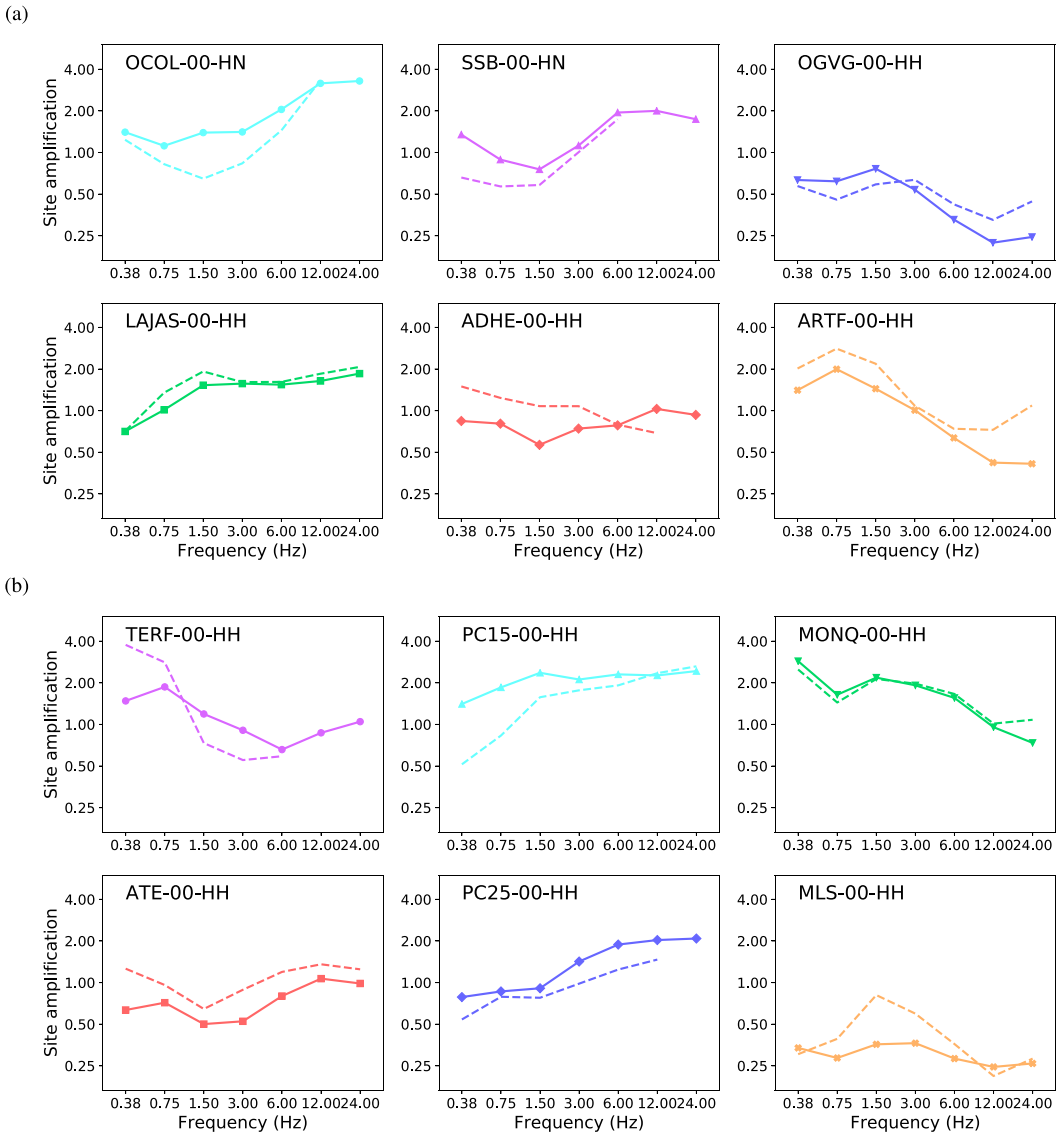

Figure 9. Energy site amplification terms $R_j(f_0)$ retrieved from envelope inversion (continuous lines) compared with the coda normalization approach $R_j^{\text{coda}}(f_0)$ (dashed lines) for stations of the Le Teil (a) and Lourdes (b) earthquakes. Site effects are relative to the selected station network.

at 0.375 Hz. Another hypothesis is that the spectra can be better explained by a double-corner frequency model (e.g. Ji & Archuleta 2021). The last hypothesis implies a complex rupture process, which has previously been invoked for moderate earthquakes with $M_w \leq 4.0$ (e.g. Uchide & Imanishi 2016).

From eq. (16) we determined stress-drops $\Delta\sigma = 3.35.10^6$ Pa and $\Delta\sigma = 9.89.10^5$ Pa for the Le Teil and Lourdes events, respectively. These values lie in the range typically found in the scientific literature (e.g. Abercrombie 1995; Ruff 1999; Allmann & Shearer 2009). For the Le Teil event, our estimate is larger than the one reported by De Novellis *et al.* (2020) ($\Delta\sigma = 1.3.10^6$ Pa) or Causse *et al.* (2021), who found $M_w = 4.85$, $f_c = 0.44$ Hz and $\Delta\sigma = 0.41.10^6$ Pa. Such differences in stress drops can be traced back to different estimates of f_c, which are amplified by the cubic exponent in eq. (16).

We also examined the effect of the propagation model on the source term by considering a non-stratified half-space model instead of the crustal waveguide presented in Fig. 2. We found that the displacement spectrum $\omega\left|\hat{M}(\omega)\right|$ is overestimated by a factor of about 2 in the 0.375–24 Hz frequency band when the velocity and heterogeneity contrasts at the Moho are neglected. This in turn implies an overestimation of the moment magnitude on the order of 0.2. This overestimation may be traced back to the stronger absorption $({}^SQ_i)^{-1}$ required to explain the coda decay at long lapse time when leakage is neglected. In this case, larger energy radiation at the source is required to compensate for the stronger attenuation of the direct arrivals while maintaining an overall good fit of the entire energy envelope.

5 CONCLUSION

We have presented a new physical approach to invert for frequency-dependent source, attenuation and site parameters from a modelling of the complete energy envelopes of seismograms between 0.375

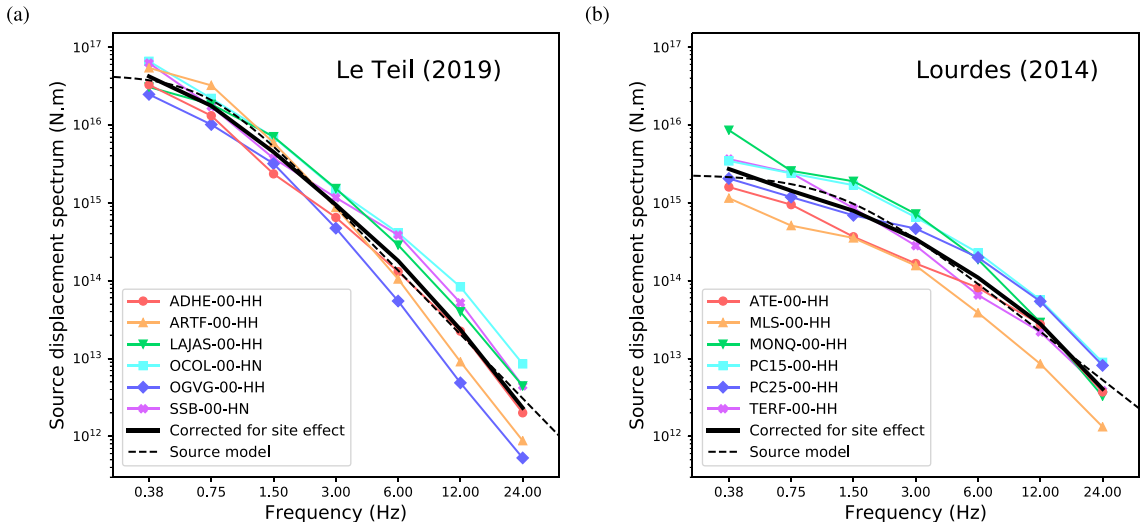

Figure 10. Source displacement spectra $|\omega\hat{M}(\omega)|$ determined from envelope inversion for the Le Teil (a) and Lourdes (b) earthquakes. The colour lines show the results uncorrected for site effects. Source displacement spectra after correction are represented by the solid black lines.

and 24 Hz, including direct *P* and *S* phases and their coda. Our approach, based on the radiative transfer theory for polarized elastic waves in a crustal waveguide geometry, models the entire envelope from direct *P*-arrivals to the late seismic *S*-coda. The 2-step inversion procedure, which first extracts attenuation parameters, then source and site contributions, combines the Levenberg–Marquardt algorithm with a grid search.

We applied our approach to two moderate events which occurred in metropolitan France: the 2019, $M_L = 5.2$ Le Teil and 2014, $M_L = 4.5$ Lourdes earthquakes. Our results show strongly frequency-dependent and moderately spatially dependent attenuation parameters with very distinguishable behaviours for scattering and absorption. Scattering attenuation dominates over absorption at sufficiently low frequency ($f < 1$–2 Hz) but decreases more rapidly than intrinsic attenuation with frequency so that the latter mechanism largely controls attenuation for $f > 3$ Hz. Although poorly resolvable, we find that the scattering mechanism is generally peaked in the forward direction, all the more so as the central frequency of the signal increases. We derived source spectra for each earthquake and estimated relevant source parameters, in particular moment magnitudes $M_w = 5.02 \pm 0.17$ and $M_w = 4.17 \pm 0.15$ for the Le Teil and Lourdes events, respectively. In the case of the Le Teil earthquake, a moderate deviation from Brune's ω^2-model was found, with an estimated spectral fall-off parameter $n = 2.73$.

Our work also illustrates that scattering anisotropy and *P*-to-*S* coupling by random heterogeneities are key in modelling the envelope of the whole seismic signal. If these effects are ignored, interesting parts of the signal cannot be modelled, such as the *P*-wave arrivals and their coda. In the case of small earthquakes, these parts of the records are often among the most energetic and could be fruitfully exploited to improve estimates of the magnitude. This issue is particularly critical in low-to-moderate seismic areas where small events represent the vast majority of earthquake catalogues.

To conclude, we would like to point out that there remains much room to improve the physical modelling of envelopes without increasing substantially the numerical effort. In particular, we have identified the excitation of surface waves as a physical process which should be taken into account in future works. First steps in this direction have been taken by (Xu *et al.* 2021) who proposed a Monte Carlo algorithm to couple body and surface waves in a multiple-scattering elastic half-space. Besides this effort, the addition of intracrustal stratification of velocity could probably improve the modelling of the direct *P* and *S* arrivals in some regions. Recent progresses have been made by Sanborn & Cormier (2018) on this aspect. The most important conclusion from our work is that the separation of path, site and source effects for moderate earthquakes based on elastic radiative transfer theory is operational and could be applied more systematically to larger data sets, thereby offering an alternative to empirical or semi-empirical approaches.

ACKNOWLEDGMENTS

We would like to thank U. Wegler and a an anonymous reviewer for their constructive criticism which helped to improve the paper. This study was part of the SIGMA-2 project funded by EDF (Électricité de France) and CEA (Commissariat à l'énergie atomique et aux énergies alternatives). This work was granted access to the HPC resources of CALMIP supercomputing centre under the allocation 2021-p20031 and the CCRT HPC resource (TOPAZE supercomputer).

SUPPORTING INFORMATION

Supplementary data are available at *GJI* online.

suppl_data

Please note: Oxford University Press is not responsible for the content or functionality of any supporting materials supplied by the authors. Any queries (other than missing material) should be directed to the corresponding author for the paper.

DATA AVAILABILITY

The data underlying this paper are provided by the French seismological and geodetic network (RESIF), at http://seismology.resif.fr/#NetworkConsultPlace:FR. This includes permanent broad-band data http://dx.doi.org/10.15778/RESIF.FR, permanent accelerometric data http://dx.doi.org/10.15778/RESIF.RA, the French Global Network of broad-band seismic stations

(GEOSCOPE) http://dx.doi.org/10.18715/GEOSCOPE.G and temporary PYROPE data http://dx.doi.org/10.15778/RESIF.X72010.

REFERENCES

Abercrombie, R.E., 1995. Earthquake source scaling relationships from- 1 to 5 ml using seismograms recorded at 2.5-km depth, *J. geophys. Res.,* **100**(B12), 24015–24036.

Aki, K., 1980. Attenuation of shear-waves in the lithosphere for frequencies from 0.05 to 25 hz, *Phys. Earth planet. Inter.,* **21**(1), 50–60.

Aki, K. & Chouet, B., 1975. Origin of coda waves: source, attenuation, and scattering effects, *J. geophys. Res.,* **80**(23), 3322–3342.

Allmann, B.P. & Shearer, P.M., 2009. Global variations of stress drop for moderate to large earthquakes, *J. geophys. Res.,* **114**(B1), doi:10.1029/2008JB005821.

Ampuero, J.P. *et al.*, 2020. The November 11 2019 Le Teil, France M5 earthquake: a triggered event in nuclear country, in *EGU General Assembly 2020,* [Online], 4-8 May 2020, EGU2020-18295.

Baker, J., Bradley, B. & Stafford, P., 2021. *Seismic Hazard and Risk Analysis,* Cambridge Univ. Press.

Braunmiller, J., Kradolfer, U., Baer, M. & Giardini, D., 2002. Regional moment tensor determination in the European–Mediterranean area—initial results, *Tectonophysics,* **356**(1–3), 5–22.

Braunmiller, J., Deichmann, N., Giardini, D. & Wiemer, S., 2005. Homogeneous moment-magnitude calibration in Switzerland, *Bull. seism. Soc. Am.,* **95**(1), 58–74.

Brune, J.N., 1970. Tectonic stress and the spectra of seismic shear waves from earthquakes, *J. geophys. Res.,* **75**(26), 4997–5009.

Calvet, M. & Margerin, L., 2013. Lapse-time dependence of Coda Q: anisotropic multiple-scattering models and application to the pyrenees, *Bull. seism. Soc. Am.,* **103**(3), 1993–2010.

Calvet, M., Sylvander, M., Margerin, L. & Villaseñor, A., 2013. Spatial variations of seismic attenuation and heterogeneity in the Pyrenees: Coda q and peak delay time analysis, *Tectonophysics,* **608,** 428–439.

Calvet, M., Margerin, L. & Hung, S.-H., 2023. Anomalous attenuation of high-frequency seismic waves in Taiwan: observation, model and interpretation, *J. geophys. Res.,* **128**(3), e2022JB025211 , doi:10.1029/2022JB025211.

Campillo, M. & Plantet, J., 1991. Frequency dependence and spatial distribution of seismic attenuation in France: experimental results and possible interpretations, *Phys. Earth planet. Inter.,* **67**(1–2), 48–64.

Cara, M. *et al.*, 2015. Si-hex: a new catalogue of instrumental seismicity for metropolitan France, *Bull. Soc. Géol. France,* **186**(1), 3–19.

Cara, M., Denieul, M., Sèbe, O., Delouis, B., Cansi, Y. & Schlupp, A., 2017. Magnitude Mw in metropolitan France, *J. Seismol.,* **21**(3), 551–565.

Causse, M., Cornou, C., Maufroy, E., Grasso, J.-R., Baillet, L. & El Haber, E., 2021. Exceptional ground motion during the shallow Mw 4.9 2019 Le Teil earthquake, France, *Commun. Earth Environ.,* **2**(1), 1–9.

Celorio, M., Chaljub, E., Margerin, L. & Stehly, L., 2022. Propagation of 2-D SH waves in random media: insights from ab initio numerical simulations and transport theory, *Front. Earth Sci.,* **10,** doi:10.3389/feart.2022.1033109.

Chevrot, S., Sylvander, M. *et al.*, 2017. Seismic network X7:PYROPE PYRenean Observational Portable Experiment (RESIF-SISMOB) [Data set]. RESIF - Réseau Sismologique et géodésique Français, doi:10.15778/RESIF.X72010.

Chevrot, S. *et al.*, 2018. The non-cylindrical crustal architecture of the Pyrenees, *Sci. Rep.,* **8**(1), 1–8.

De Novellis, V., Convertito, V., Valkaniotis, S., Casu, F., Lanari, R., Tobar, M. F.M. & Pino, N.A., 2020. Coincident locations of rupture nucleation during the 2019 Le Teil earthquake, france and maximum stress change from local cement quarrying, *Commun. Earth Environ.,* **1**(1), 1–10.

Deichmann, N., 2006. Local magnitude, a moment revisited, *Bull. seism. Soc. Am.,* **96**(4A), 1267–1277.

Delouis, B., Oral, E., Menager, M., Ampuero, J.-P., Trilla, A.G., Régnier, M. & Deschamps, A., 2021. Constraining the point source parameters of the 11 November 2019 Mw 4.9 Le Teil earthquake using multiple relocation approaches, first motion and full waveform inversions, *Comp. Rend. Géosci.,* **353**(S1), 1–24.

Denieul, M., Sèbe, O., Cara, M. & Cansi, Y., 2015. M w estimation from crustal coda waves recorded on analog seismograms, *Bull. seism. Soc. Am.,* **105**(2A), 831–849.

Drouet, S., Cotton, F. & Guéguen, P., 2010. v s 30, κ, regional attenuation and m w from accelerograms: application to magnitude 3–5 French earthquakes, *Geophys. J. Int.,* **182**(2), 880–898.

Duverger, C., Mazet-Roux, G., Bollinger, L., Guilhem Trilla, A., Vallage, A., Hernandez, B. & Cansi, Y., 2021. A decade of seismicity in metropolitan France (2010–2019): the CEA/LDG methodologies and observations, *BSGF-Earth Sci. Bull.,* **192**(1), doi:10.1051/bsgf/2021014.

Eken, T., 2019. Moment magnitude estimates for central Anatolian earthquakes using coda waves, *Solid Earth,* **10**(3), 713–723.

Eulenfeld, T. & Wegler, U., 2016. Measurement of intrinsic and scattering attenuation of shear waves in two sedimentary basins and comparison to crystalline sites in Germany, *Geophys. J. Int.,* **205**(2), 744–757.

Eulenfeld, T. & Wegler, U., 2017. Crustal intrinsic and scattering attenuation of high-frequency shear waves in the contiguous united states, *J. geophys. Res.,* **122**(6), 4676–4690.

Eulenfeld, T., Dahm, T., Heimann, S. & Wegler, U., 2022. Fast and robust earthquake source spectra and moment magnitudes from envelope inversion, *Bull. seism. Soc. Am.,* **112**(2), 878–893.

Fehler, M., Hoshiba, M., Sato, H. & Obara, K., 1992. Separation of scattering and intrinsic attenuation for the Kanto-Tokai region, japan, using measurements of S-wave energy versus hypocentral distance, *Geophys. J. Int.,* **108**(3), 787–800.

Gaebler, P.J., Eulenfeld, T. & Wegler, U., 2015. Seismic scattering and absorption parameters in the w-bohemia/vogtland region from elastic and acoustic radiative transfer theory, *Geophys. Suppl. Mon. Not. R. astron. Soc.,* **203**(3), 1471–1481.

Galassi, M. *et al.*, 2002. *GNU Scientific Library,* Network Theory Limited Godalming.

Gusev, A. & Abubakirov, I., 1987. Monte-carlo simulation of record envelope of a near earthquake, *Phys. Earth planet. Inter.,* **49**(1–2), 30–36.

Gusev, A. & Abubakirov, I., 1999. Vertical profile of effective turbidity reconstructed from broadening of incoherent body-wave pulses—I. General approach and the inversion procedure, *Geophys. J. Int.,* **136**(2), 295–308.

Hanks, T.C. & Kanamori, H., 1979. A moment magnitude scale, *J. geophys. Res.,* **84**(B5), 2348–2350.

Heller, G., 2021. Vers une meilleure estimation de la magnitude à partir de la coda sismique, *PhD thesis*, IRAP.

Heller, G., Margerin, L., Sèbe, O., Mayor, J. & Calvet, M., 2022. Revisiting multiple-scattering principles in a crustal waveguide: equipartition, depolarization and coda normalization, *Pure appl. Geophys.,* **179,** 2031–2065.

Hoshiba, M., 1994. Simulation of coda wave envelope in depth dependent scattering and absorption structure, *Geophys. Res. Lett.,* **21**(25), 2853–2856.

Hoshiba, M., 1995. Estimation of nonisotropic scattering in western Japan using coda wave envelopes: application of a multiple nonisotropic scattering model, *J. geophys. Res.,* **100**(B1), 645–657.

Ji, C. & Archuleta, R.J., 2021. Two empirical double-corner-frequency source spectra and their physical implications, *Bull. seism. Soc. Am.,* **111**(2), 737–761.

Jing, Y., Zeng, Y. & Lin, G., 2014. High-frequency seismogram envelope inversion using a multiple nonisotropic scattering model: application to aftershocks of the 2008 wells earthquake, *Bull. seism. Soc. Am.,* **104**(2), 823–839.

Kanamori, H., 1977. The energy release in great earthquakes, *J. geophys. Res.,* **82**(20), 2981–2987.

Kaneko, Y. & Shearer, P.M., 2014. Seismic source spectra and estimated stress drop derived from cohesive-zone models of circular subshear rupture, *Geophys. J. Int.,* **197**(2), 1002–1015.

Korn, M., 1990. A modified energy flux model for lithospheric scattering of teleseismic body waves, *Geophys. J. Int.,* **102**(1), 165–175.

Lacombe, C., Campillo, M., Paul, A. & Margerin, L., 2003. Separation of intrinsic absorption and scattering attenuation from *Lg* coda decay in

central France using acoustic radiative transfer theory, *Geophys. J. Int.,* **154**(2), 417–425.

Lee, W.S., Sato, H. & Lee, K., 2003. Estimation of S-wave scattering coefficient in the mantle from envelope characteristics before and after the *ScS* arrival, *Geophys. Res. Lett.,* **30**(24), doi:10.1029/2003GL018413.

Mancinelli, N., Shearer, P. & Liu, Q., 2016. Constraints on the heterogeneity spectrum of Earth's upper mantle, *J. geophys. Res.,* **121**(5), 3703–3721.

Margerin, L., 2005. Introduction to radiative transfer of seismic waves, in *Seismic Earth: Array Analysis of Broadband Seismograms,* Vol. **157,** Geophysical Monograph Series, eds Levander, A. & Nolet, G., AGU.

Margerin, L., Campillo, M. & Tiggelen, B., 1998. Radiative transfer and diffusion of waves in a layered medium: new insight into Coda Q, *Geophys. J. Int.,* **134**(2), 596–612.

Margerin, L., Campillo, M., Shapiro, N. & van Tiggelen, B., 1999. Residence time of diffuse waves in the crust as a physical interpretation of Coda Q: application to seismograms recorded in mexico, *Geophys. J. Int.,* **138**(2), 343–352.

Margerin, L., Campillo, M. & Van Tiggelen, B., 2000. Monte Carlo simulation of multiple scattering of elastic waves, *J. geophys. Res.,* **105**(B4), 7873–7892.

Margerin, L., Campillo, M., Van Tiggelen, B. & Hennino, R., 2009. Energy partition of seismic coda waves in layered media: theory and application to pinyon flats observatory, *Geophys. J. Int.,* **177**(2), 571–585.

Mayeda, K. & Walter, W.R., 1996. Moment, energy, stress drop, and source spectra of western United States earthquakes from regional coda envelopes, *J. geophys. Res.,* **101**(B5), 11195–11208.

Mayeda, K., Hofstetter, A., O'Boyle, J.L. & Walter, W.R., 2003. Stable and transportable regional magnitudes based on coda-derived moment-rate spectra, *Bull. seism. Soc. Am.,* **93**(1), 224–239.

Mayor, J., Margerin, L. & Calvet, M., 2014. Sensitivity of coda waves to spatial variations of absorption and scattering: radiative transfer theory and 2-D examples, *Geophys. J. Int.,* **197**(2), 1117–1137.

Mayor, J., Calvet, M., Margerin, L., Vanderhaeghe, O. & Traversa, P., 2016. Crustal structure of the Alps as seen by attenuation tomography, *Earth planet. Sci. Lett.,* **439,** 71–80.

Mayor, J., Traversa, P., Calvet, M. & Margerin, L., 2018. Tomography of crustal seismic attenuation in metropolitan France: implications for seismicity analysis, *Bull. Earthq. Eng.,* **16**(6), 2195–2210.

Mazzotti, S., Aubagnac, C., Bollinger, L., Oscanoa, K.C., Delouis, B. & Do Paco, D., 2021. FMHex20: a database of earthquake focal mechanisms in metropolitan France and conterminous western Europe, *BSGF–Earth Sci. Bull.,* **192**(9), doi:10.1051/bsgf/2020049.

Menina, S. *et al.*, 2021. Energy envelope and attenuation characteristics of high-frequency (HF) and very-high-frequency (VF) martian events, *Bull. seism. Soc. Am.,* **111**(6), 3016–3034.

Menina, S. *et al.*, 2023. Stratification of heterogeneity in the lithosphere of Mars from envelope modeling of event S1222a and near impacts: interpretation and implications for very-high-frequency events, *Geophys. Res. Lett.,* **50**(7), e2023GL103202.

Pasyanos, M.E., Gök, R. & Walter, W.R., 2016. 2d variations in coda amplitudes in the middle east, *Bull. seism. Soc. Am.,* **106**(5), 1915–1925.

Phillips, W.S. & Aki, K., 1986. Site amplification of coda waves from local earthquakes in central California, *Bull. seism. Soc. Am.,* **76**(3), 627–648.

Picozzi, M., Oth, A., Parolai, S., Bindi, D., De Landro, G. & Amoroso, O., 2017. Accurate estimation of seismic source parameters of induced seismicity by a combined approach of generalized inversion and genetic algorithm: application to the Geysers Geothermal Area, California, *J. geophys. Res.,* **122**(5), 3916–3933.

Pondrelli, S., Morelli, A., Ekström, G., Mazza, S., Boschi, E. & Dziewonski, A., 2002. European–Mediterranean regional centroid-moment tensors: 1997–2000, *Phys. Earth planet. Inter.,* **130**(1–2), 71–101.

Przybilla, J., Wegler, U. & Korn, M., 2009. Estimation of crustal scattering parameters with elastic radiative transfer theory, *Geophys. J. Int.,* **178**(2), 1105–1111.

Rautian, T. & Khalturin, V., 1978. The use of the coda for determination of the earthquake source spectrum, *Bull. seism. Soc. Am.,* **68**(4), 923–948.

RESIF, 1995a. Resif-rap French accelerometric network, *RESIF – Réseau Sismologique et géodésique Français* , doi:10.15778/resif.ra.

RESIF, 1995b. Resif-rlbp french broad-band network, resif-rap strong motion network and other seismic stations in metropolitan France, *RESIF – Réseau Sismologique et géodés, ique Français* , doi:10.15778/resif.fr.

Richter, C.F., 1935. An instrumental earthquake magnitude scale, *Bull. seism. Soc. Am.,* **25**(1), 1–32.

Ritz, J.-F., Baize, S., Ferry, M., Larroque, C., Audin, L., Delouis, B. & Mathot, E., 2020. Surface rupture and shallow fault reactivation during the 2019 Mw 4.9 Le Teil earthquake, France, *Commun. Earth Environ.,* **1**(1), 1–11.

Romanowicz, B., Cara, M., Fel, J.F. & Rouland, D., 1984. Geoscope: A french initiative in long-period three-component global seismic networks, *Eos, Transactions American Geophysical Union,* **65**(42), 753–753.

Ruff, L.J., 1999. Dynamic stress drop of recent earthquakes: variations within subduction zones, in *Seismogenic and Tsunamigenic Processes in Shallow Subduction Zones,* pp. 409–431, Springer.

Ryzhik, L., Papanicolaou, G. & Keller, J.B., 1996. Transport equations for elastic and other waves in random media, *Wave Motion,* **24**(4), 327–370.

Sanborn, C.J. & Cormier, V.F., 2018. Modelling the blockage of lg waves from three-dimensional variations in crustal structure, *Geophys. J. Int.,* **214**(2), 1426–1440.

Sato, H., 1984. Attenuation and envelope formation of three-component seismograms of small local earthquakes in randomly inhomogeneous lithosphere, *J. geophys. Res.,* **89**(B2), 1221–1241.

Sato, H., 1989. Broadening of seismogram envelopes in the randomly inhomogeneous lithosphere based on the parabolic approximation: southeastern Honshu, Japan, *J. geophys. Res.,* **94**(B12), 17735–17747.

Sato, H., 2019. Power spectra of random heterogeneities in the solid earth, *Solid Earth,* **10**(1), 275–292.

Sato, H., Fehler, M.C. & Maeda, T., 2012. *Seismic Wave Propagation and Scattering in the Heterogeneous Earth,* Vol. **496,** Springer.

Schlupp, A., Sira, C., Maufroy, E., Provost, L., Dretzen, R., Bertrand, E., Beck, E. & Schaming, M., 2021. Ems98 intensities distribution of the "Le Teil" earthquake, France, 11 November 2019 (Mw 4.9) based on macroseismic surveys and field investigations, *Comp. Rend. Géosci.,* **353**(S1), 1–28.

Sens-Schönfelder, C. & Wegler, U., 2006. Radiative transfer theory for estimation of the seismic moment, *Geophys. J. Int.,* **167**(3), 1363–1372.

Sens-Schönfelder, C., Margerin, L. & Campillo, M., 2009. Laterally heterogeneous scattering explains Lg blockage in the Pyrenees, *J. geophys. Res.,* **114**(B7), doi:10.1029/2008JB006107.

Shearer, P., 1999. *Introduction to Seismology,* 2nd edn, Cambridge Univ. Press.

Shelly, D.R. *et al.*, 2021. A big problem for small earthquakes: benchmarking routine magnitudes and conversion relationships with coda envelope-derived Mw in southern Kansas and northern Oklahoma, *Bull. seism. Soc. Am,* **112**(1), 210–225.

Sira, C., Schlupp, A. & Schaming, M., 2016. Séisme de La Rochelle (Charente-Maritime) du 28 avril 2016, à 6h46 TUMagnitude: 4,9 (ML RéNaSS), *PhD thesis*, Université de Strasbourg, CNRS.

Souriau, A., Rigo, A., Sylvander, M., Benahmed, S. & Grimaud, F., 2014. Seismicity in central-western Pyrenees (France): a consequence of the subsidence of dense exhumed bodies, *Tectonophysics,* **621,** 123–131.

Takahashi, T., Sato, H., Ohtake, M. & Obara, K., 2005. Scale dependence of apparent stress for earthquakes along the subducting Pacific Plate in northeastern Honshu, Japan, *Bull. seism. Soc. Am.,* **95**(4), 1334–1345.

Takahashi, T., Sato, H., Nishimura, T. & Obara, K., 2009. Tomographic inversion of the peak delay times to reveal random velocity fluctuations in the lithosphere: method and application to northeastern Japan, *Geophys. J. Int.,* **178**(3), 1437–1455.

Takemura, S., Kobayashi, M. & Yoshimoto, K., 2016. Prediction of maximum P- and S-wave amplitude distributions incorporating frequency-and

distance-dependent characteristics of the observed apparent radiation patterns, *Earth, Planets Space,* **68**(1), 1–9.

Takeuchi, N., 2016. Differential Monte Carlo method for computing seismogram envelopes and their partial derivatives, *J. geophys. Res.,* **121**(5), 3428–3444.

Tsujiura, M., 1978. Spectral analysis of the coda waves from local earthquakes, *Bull. Earthq. Res. Inst,* **53,** 1–48.

Turner, J.A., 1998. Scattering and diffusion of seismic waves, *Bull. seism. Soc. Am.,* **88**(1), 276–283.

Uchide, T. & Imanishi, K., 2016. Small earthquakes deviate from the omega-square model as revealed by multiple spectral ratio analysis, *Bull. seism. Soc. Am.,* **106**(3), 1357–1363.

Vacher, P. & Souriau, A., 2001. A three-dimensional model of the pyrenean deep structure based on gravity modelling, seismic images and petrological constraints, *Geophys. J. Int.,* **145**(2), 460–470.

Vallage, A. *et al.*, 2021. Multitechnology characterization of an unusual surface rupturing intraplate earthquake: the M_L 5.4 2019 Le Teil event in France, *Geophys. J. Int.,* **226**(2), 803–813.

Wang, W. & Shearer, P., 2017. Using direct and coda wave envelopes to resolve the scattering and intrinsic attenuation structure of southern California, *J. geophys. Res.,* **122**(9), 7236–7251.

Wang, W. & Shearer, P.M., 2019. An improved method to determine CODA-Q, earthquake magnitude, and site amplification: theory and application to southern California, *J. geophys. Res.,* **124**(1), 578–598.

Weaver, R.L., 1990. Diffusivity of ultrasound in polycrystals, *J. Mech. Phys. Solids,* **38**(1), 55–86.

Xu, Z., Margerin, L. & Mikesell, T.D., 2021. Monte Carlo simulations of coupled body- and Rayleigh-wave multiple scattering in elastic media, *Geophys. J. Int,* **228**(2), 1213–1236.